Exploring the Synthesis and Optoelectronic Properties of $Cs_2AgSb_xBi_{1-x}Br_6$ Double Perovskites

Sohan Abhay Phadke

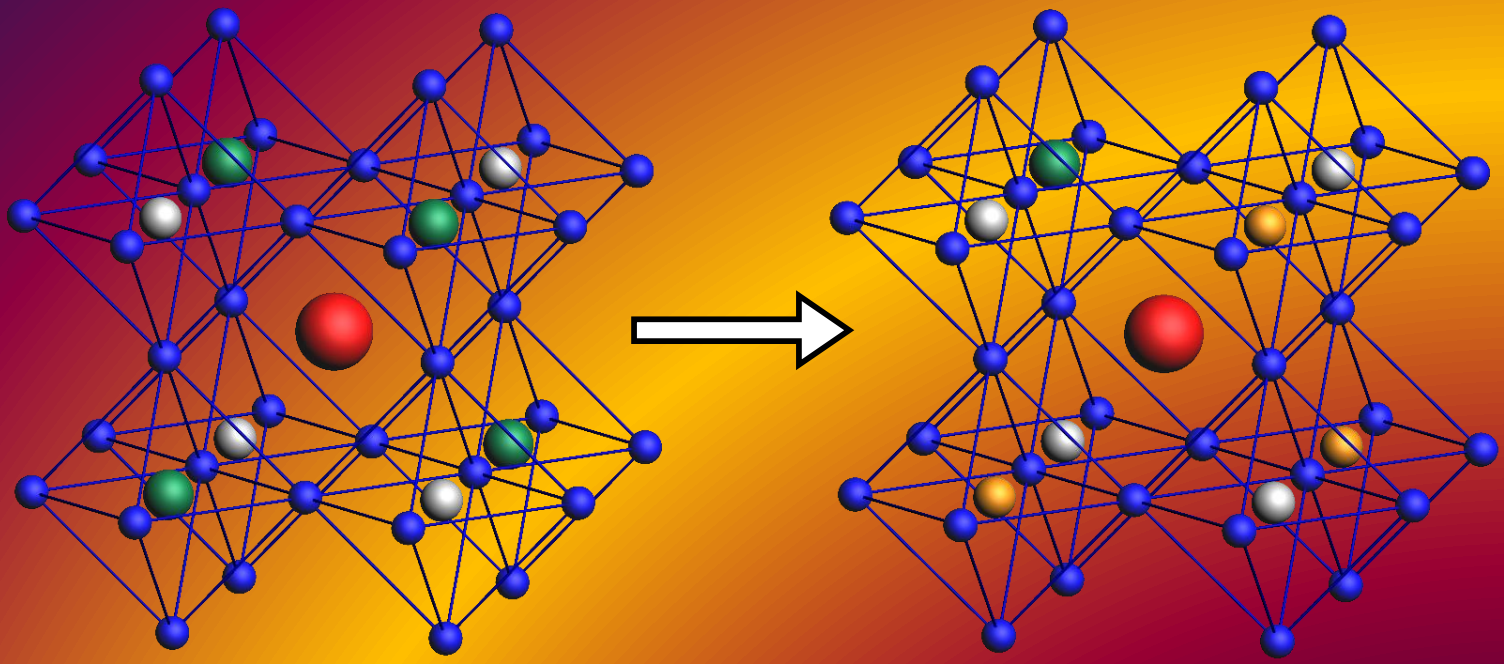

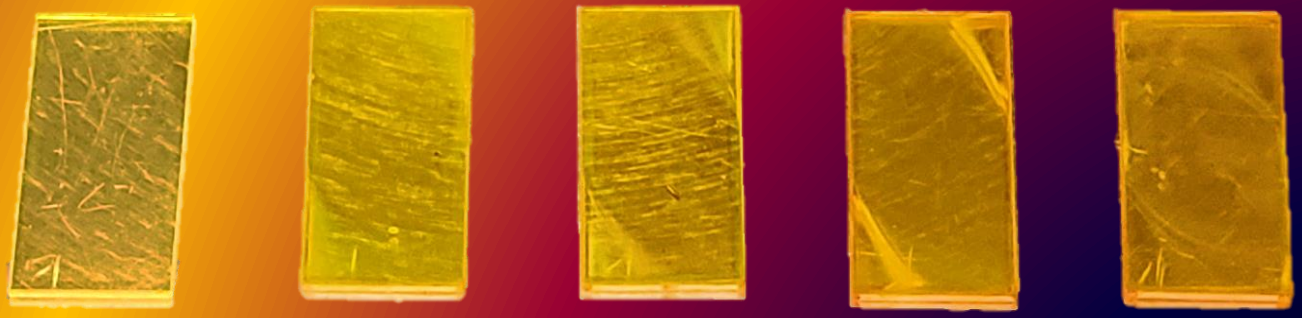

TU Delft

Exploring the Synthesis and Optoelectronic Properties of $Cs_2AgSb_xBi_{1-x}Br_6$ Double Perovskites

A Combined Computational and Experimental Study

by

Sohan Abhay Phadke

to obtain the degree of Master of Science
at the Delft University of Technology,
to be defended publicly on Monday, August 31, 2020 at 1:30 PM.

Student number: 4829212
Project duration: January 6, 2020 – August 31, 2020
Thesis committee:

Dr. ir. T. J. Savenije,	TU Delft, supervisor
Prof. Dr. F. C. Grozema,	TU Delft
Prof. Dr. S. J. Picken,	TU Delft

TU Delft

Preface

This report contains a detailed account of the work performed in the laboratory of Professor Tom J. Savenije under the daily supervision of Valentina Caselli for the fulfillment of the requirements for the degree of Master of Science. I would like to thank both Tom and Valentina for their guidance and tutelage during this thesis project, as well as for their advice future concerning career paths. Special thanks are extended to Professor Ferdinand C. Grozema for his guidance concerning Density Functional Theory and for essentially adopting me as a Master's student in his group. Thanks are also extended to Duco Bosma for SEM/EDXS measurements. I would also like to extend my sincere gratitude to all members of the Optoelectronic Materials group who have helped shape both the contents of this report and my professional development through countless hours of discussion, experimentation, and assistance.

I would like to thank my family for their continued and unconditional love and support from the other side of the world. I am extremely fortunate to be a part of such a loving family and hope that I continue to earn the love and support they have given me. I would also like to thank my friends and colleagues for providing a wonderful learning and living experience during these past two years. Lastly, I would like to thank Laura Donk for providing me with continuous motivation throughout this work.

Sohan Abhay Phadke
Delft, August 2020

Summary

Perovskite photovoltaic (PV) cells have become one of the most highly researched topics in photovoltaics and have achieved unprecedented increases in device efficiencies, but their commercialization remains hindered by their low stability and high toxicity. The currently best-performing perovskite PV cells contain lead, a neurotoxic material whose use is prohibited under many national consumer protection laws, thus impeding adoption by industry. A class of materials called double perovskites offer an elegant pathway to lead-free, low-toxicity perovskites for PV cell applications by replacing the Pb^{2+} cation in the perovskite with a mixture of charge 1+ and 3+ cations. A promising double perovskite, $Cs_2AgBiBr_6$, was first synthesized in 2016 and has been used in the fabrication of PV devices with efficiencies of $\leq$2.5%. While numerous research groups have attempted various synthesis routes and produced various final materials, little is known about the dynamics of the double perovskite synthesis or the effect of further metal substitution on the material's optoelectronic properties. In this work, the solution phase synthesis of $Cs_2AgBiBr_6$ was studied via Density Functional Theory (DFT) and the optoelectronic properties of $Cs_2AgSb_xBi_{1-x}Br_6$ thin films were explored, with antimony substitution presented as a method to lower the band gap to make a more favorable perovskite for PV cell applications.

The synthesis method of the thin films involved mixing all of the precursors in DMSO solvent and spin coating. However, only $BiBr_3$ and $SbBr_3$ were found to dissolve individually in solution, indicating a sequential pathway to double perovskite crystallites in solution. Geometry optimizations of Bi-Br-DMSO complexes were performed via DFT using the BLYP functional, with COSMO used to approximate a solution phase system. While COSMO was found to be incompatible with the corrected method of calculating the interaction energy, the relatively low (~11%) basis set superposition error was accepted and the uncorrected calculation method was used to find the most stable Bi-Br-DMSO complexes in solution. These complexes were analyzed using TD-DFT and the CAM-B3LYP functional to simulate absorbance spectra and match them to experimental solution spectra. While one of the transitions at ~3.9 eV may be ascribed to a larger cluster of $[Bi_4Br_{20}]^{8-}$, the source of the stronger experimental transition at ~3.5 eV could not be determined. The dominant electronic transition of the Bi-Br-DMSO system was a metal-to-ligand charge transfer from the $6s$ orbital of the central bismuth ion to the $3p$ orbital of the bromine ligand.

A facile synthesis method reported in literature was attempted for the synthesis of $Cs_2AgSb_xBi_{1-x}Br_6$ thin films, described briefly above. The method was found to produce thin films of high crystallinity but with a tendency to degrade upon exposure to ambient conditions, as evidenced by x-ray diffraction (XRD) measurements. A reduced annealing temperature of 90°C rather than 250°C led to the successful substitution of Sb^{3+} for Bi^{3+} in the double perovksite while simultaneously avoiding material degradation (at the cost of optoelectronic performance). Shifts in the lattice parameter of ~0.05 Å and shifts in the absorbance onset energy of ~0.2 eV were found by XRD and absorbance measurements, respectively, for antimony replacement of up to x = 0.7. The optoelectronic properties of the materials were studied using time-resolved microwave conductivity (TRMC) measurements, and showed a decrease in photoconductance of two orders of magnitude and a reduction of charge carrier lifetime as the annealing temperature was lowered from 250°C to 90°C. Low temperature absorbance measurements combined with TRMC measurements indicated that the peak in the absorbance spectra was most likely the result of an excitonic transition.

Contents

1 Introduction

The Energy Transition

Fossil fuels are predicted to be exhausted within a century and new, renewable energy technologies will have to be found in order to maintain current energy consumption. Photovoltaic (PV) cells, devices that convert solar energy directly to electricity, are a renewable energy technology with the capacity to help usher in the transition. They have the advantages of having no moving parts and requiring very little maintenance over the product's lifespan in comparison with mechanical renewable energy technologies such as wind turbines or hydroelectric power stations. However, the fabrication of PV cells in a chemical factory can be very costly and very energy-intensive, with the majority of PV cells in production based on silicon. As the need for new, cost-effective renewable energy technologies increases, new solar energy absorber materials must be explored.

Current Solar Energy Market

Silicon was one of the first materials to be used to be used as a solar energy absorber material, with the first practically viable PV cell created at Bell Labs in 1954 [1]. Silicon has remained the dominant material in the PV industry and has been labeled as a first-generation material. As decades have passed, the price of silicon PV cells (in terms of cost per kW) has steadily decreased as the technology has matured. However, their manufacture is still energy-intensive, requiring high temperatures to form highly crystalline silicon ingots. The so-called second-generation materials were an attempt to bring the cost per kW ratio even lower by employing thin film materials such as cadmium telluride or gallium arsenide. While the cost of the panels was lowered, the cost per kW was not significantly decreased, because the efficiency of the devices was not high enough. This has led to the pursuit of third-generation materials, which are solar energy absorber materials that are both cheap and highly efficient [2]. One candidate that has been found is a class of materials called perovskites, which have seen an unprecedented rise in research-cell efficiencies in the short time since their invention. Perovskites are also an attractive material due to their ease of processability, with low-energy methods such as vapor deposition and roll-to-roll processing used in the large scale manufacture of perovskite PV cells.

Perovskite PV Cells

Perovskites are a class of materials with the same crystal structure as that of $CaTiO_3$ and the chemical formula ABX_3. In semiconductor perovskites, A is typically a small cation (methylammonium, formamidinium, cesium), B is a charge 2+ cation (lead, tin), and X is a halide (bromide, iodide) [3]. The crystal structure of a perovskite, $CsPbBr_3$, is shown in Figure 1.1a). The unit cell is a cubic unit cell with a multi-atom basis, with B at (0, 0, 0), A at (1/2, 1/2, 1/2), and X at (1/2, 0, 0), (0, 1/2, 0), and (0, 0, 1/2). It is often more conveniently discussed as in Figure 1.1b), with A sitting in the space shared between eight BX_6 octahedra.

Since their introduction as solar energy absorber materials in 2012, the efficiency of perovskite PV cells has increased faster than any other PV technology, with record cell efficiencies surpassing those of industrially available silicon PV cells [4–6]. The meteoric rise in research cell efficiencies is often attributed to the interesting and unique properties that these materials have such as tunable band gaps

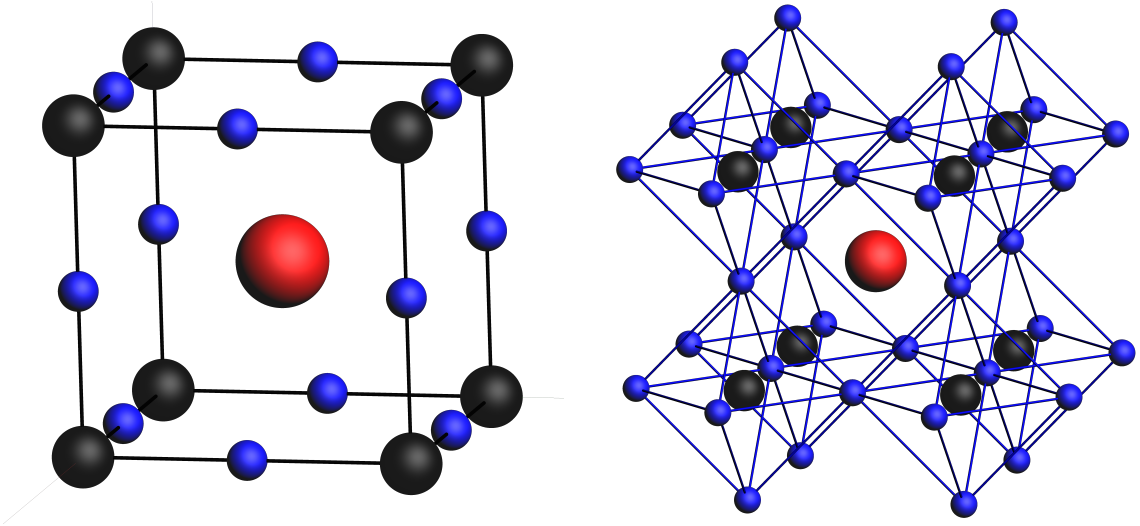

(a) The standard unit cell. (b) The structure in the form it is usually discussed.

Figure 1.1: Crystal structures of $CsPbBr_3$, where Red = Cs, Black = Pb, Blue = Br.

via halide substitution, favorably sized and direct band gaps, tolerance of defects in the final films, high charge carrier mobilities, and high attenuation coefficients in the usable portion of the solar spectrum [7]. Consequently, perovskites have become one of the most highly researched materials in the field of semiconductors, contributing to over 9,000 research articles in the year 2019.

However, to date, very few companies manufacture perovskite PV cells industrially (with the most famous example, Oxford PV, using perovskites as a top cell in silicon-perovskite tandem PV cells) [8]. One factor contributing to the slow uptake of perovskites in industrial production are that perovskites are unstable in the presence of moisture and O_2, thus requiring either excellent encapsulation or high levels of materials engineering to improve stability [9]. The second main factor limiting their adoption in industry is that the best performing perovskite PV cells typically contain lead as a charge 2+ cation in the material. Pb^{2+} is soluble in water and is known for its high neurotoxicity, with many national laws prohibiting the use of lead-containing materials in consumer products [10–12].

Double Perovskites

A few options have been suggested to replace Pb^{2+} in perovskites, such as substituting Pb^{2+} for Sn^{2+}. However, Sn^{2+} oxidizes to Sn^{4+}, resulting in degradation of the perovskite material [13, 14]. A more elegant solution is to replace Pb^{2+} by alternating cations of charge 1+ and 3+, such as in $Cs_2AgBiBr_6$. This material was first synthesized by Slavney et al. in 2016, and is called a double perovskite [15]. A double perovskite is a material with chemical formula $A_2B'B''X_6$, where B' and B" are transition metal cations with charge 1+ and 3+, respectively. XRD experiments by Slavney et al. confirmed the structure was similar to that of standard cubic perovskites, thus indicating that in order to maintain charge neutrality, the double perovskite featured Ag^{1+} and Bi^{3+} in alternating order occupying the position previously held by Pb^{2+}, as in Figure 1.2a).

PV cells have maximum fundamental device efficiencies of ~33% conversion of solar energy to usable electricity as found by William Shockley and Hans Quiesser in their seminal paper from 1960 [16]. This occurs at an ideal band gap energy of 1.34 eV, which is quite far from the 2.2 eV band gap of $Cs_2AgBiBr_6$ [17]. Substitution of Sb^{3+} for Bi^{3+} has been shown to decrease the band gap energy while maintaining charge transport, which could provide a pathway to high-efficiency, lead-free perovskite PV cells [18]. The crystal structure of an antimony substituted silver-bismuth double perovskite is shown in Figure 1.2b).

The $Cs_2AgBiBr_6$ double perovskite first synthesized by Slavney et al. was in the form of 1 mm single crystals. Soon afterwards, $Cs_2AgBiBr_6$ was synthesized as a powder by sintering precursors under vacuum by Du et al., and via ball milling by Garcia-Espejo et al. [19, 20]. Thin film double perovskite PV devices of low efficiencies (<2.5%) have also been created via solution processed and vapor deposited routes using the same material [21–24]. Ionic substitution in $Cs_2AgBiBr_6$ has also

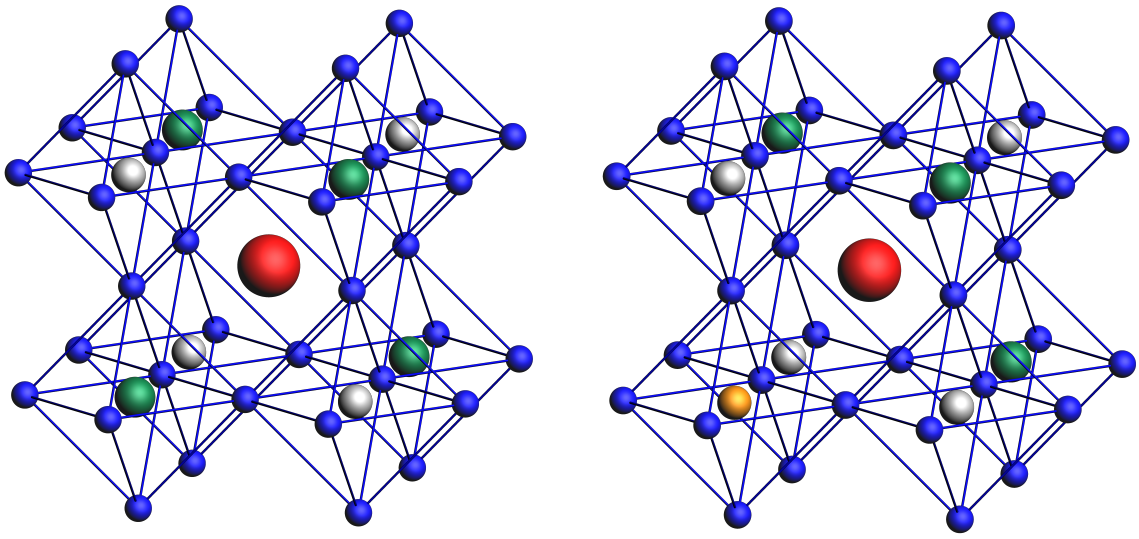

(a) The lead-free double perovskite, analogous to Figure 1.1b), with alternating Ag^{1+} and Bi^{3+} ions replacing Pb^{2+}.

(b) An extension of the double perovskite with further metal ion substitution of Sb^{3+} for Bi^{3+} at x = 0.25.

Figure 1.2: Crystal structures of $Cs_2AgSb_xBi_{1-x}Br_6$, where Red = Cs, Gray = Ag, Orange = Sb, Green = Bi, Blue = Br. Ag^{1+} and Bi^{3+} replace Pb^{2+} in alternating order for an average charge of 2+ from the B cation.

been accomplished, substituting Sb^{3+} for Bi^{3+} by García-Espejo et al. in powders and very recently by Li et al. and Liu et al. in thin films [20, 25, 26]. However, despite the variety of synthesis routes and final materials prepared, little is known about the underlying physics of the material.

Thesis Objectives and Outline

While still a relatively new material, $Cs_2AgSb_xBi_{1-x}Br_6$ has already been used to make PV devices. However, the efficiency of <2.5% does not reach the aim of third-generation PV materials in terms of cost per kW of electricity produced. In order to understand why, further study of its synthesis and optoelectronic properties must be performed. Understanding the steps of the synthesis will allow for a more precise and informed fabrication method with greater control of the optoelectronic properties. Examination of the optoelectronic properties of current $Cs_2AgSb_xBi_{1-x}Br_6$ thin films will allow for an understanding of the principle sources of defects and issues with the material that prevent maximum energy conversion.

Chapter 2 describes the underlying fundamental theories of the work presented in this thesis, while Chapter 3 describes the specific methods and equipment used. Concerning the synthesis, this work specifically aims to address the question of which complexes are formed in the precursor spin coating solution and what is the pathway to the final double perovskite. As will be discussed in Chapter 4.1, the precursor materials were found to dissolve in a specific sequence, indicating their successive addition to a complex in solution. Understanding precisely what the complex is could allow for better tuning of the final film. Analysis of the precursors in solution was performed using Density Functional Theory (DFT) and Time-Dependent Density Functional Theory (TD-DFT) calculations of their absorbance spectra. These simulated spectra were compared with experimental solution spectra to try and ascertain which complexes are present in solution. Concerning the optoelectronic characterization, the effect of antimony substitution is still not fully understood. Chapter 4.2 begins by first examining the structural and optoelectronic properties of $Cs_2AgBiBr_6$ thin films, including the often-noted peak in the absorbance spectra. The primary methods used for analysis were XRD measurements for structural characterization and TRMC measurements for optoelectronic characterization. This analysis was then repeated for $Cs_2AgSb_xBi_{1-x}Br_6$ thin films.

2

Theory

2.1. Semiconductor Physics

2.1.1. Band Theory

Molecular Orbital (MO) Theory explains that as atoms come together to form molecules, their bonding can be explained by the formation of bonding and antibonding molecular orbitals, with the lower energy bonding MO's typically being filled with electrons [27]. The highest energy orbital that is occupied with electrons is referred to as the Highest Occupied Molecular Orbital (HOMO), and the lowest energy orbital that is unoccupied with electrons is referred to as the Lowest Unoccupied Molecular Orbital (LUMO). As the number of atoms increases, the number of molecular orbitals also increases, with the bonding MO's being filled with the electrons of the component atoms. As the size of the system increases from a single molecule to a bulk crystal, the energy spacing between multiple bonding and multiple antibonding orbitals decreases to energies less than the ambient thermal energy (spacing of 10^{-19} eV versus k_BT = 0.0259 eV), leading to what are known as bands (see Figure 2.1). The lower energy band is called the valence band, so named as it contains the valence electrons of the atoms in the bulk crystal, and the higher energy band is called the conduction band, so named as an electron in this band can move freely to conduct electricity. The difference in energy between the two bands is known as the band gap, and becomes smaller as the size of the system increases from a single molecule to a bulk crystal. In a perfect crystal, no electron states can exist within the band gap.

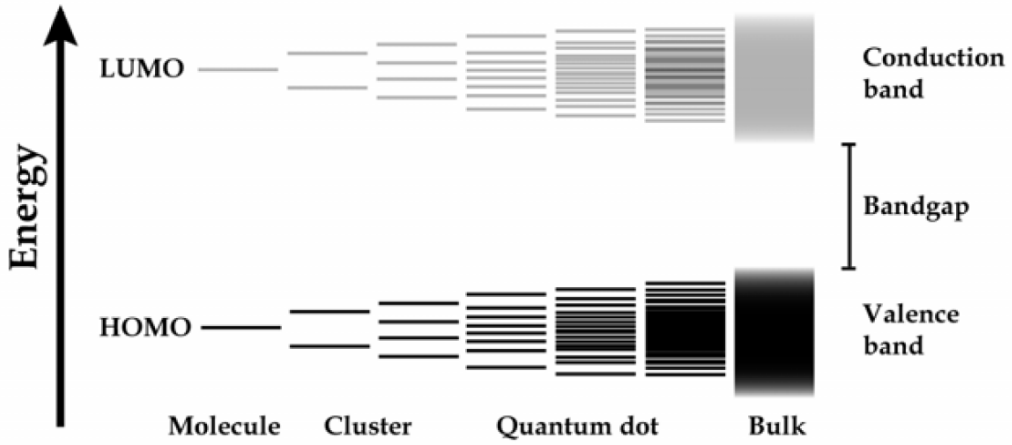

Figure 2.1: A diagram showing the density of available electron energy states as the size of the system increases. Thin films are generally considered to be in the bulk regime [28].

2.1.2. Electronic Excitation and Recombination

Excitation

Electrons can be excited from the valence band to the conduction band by light of energy greater than or equal to the band gap, leaving behind a positively charged quasiparticle called a hole. Photons of energy lower than the band gap will pass through the material without exciting an electron. Photons with energy greater than the band gap will excite an electron to an energy higher than the conduction band edge, where that electron will then thermally relax to the edge of the conduction band by dissipating excess energy as heat. Electrons and holes are referred to as charge carriers as they are both capable of moving through the bulk semiconductor with charge of $\pm e$.

Recombination

Electrons in the conduction band can fall back to the valence band via multiple pathways. There are three dominant mechanisms for carrier recombination: band-to-band recombination, trap-assisted recombination, and Auger recombination (see Figure 2.2). The mechanisms are called recombination because they involve a free electron and hole joining to annihilate each other. In band-to-band recombination, the excited state electron falls to the conduction band while simultaneously emitting a photon of energy equivalent to the transition. This process is unimolecular and is responsible for photoluminescence. In trap-assisted recombination, a trap state (an energy level appearing in the band gap due to structural defect or atomic substitution), acts as an intermediary. Rather than the excited electron needing to emit light to fall back to ground state, both the electron and hole move to the trap state, annihilating each other in a bimolecular process. This process can also be thought of as a first-order process, if the charge carriers have separated and only one recombines with a defect in the material (thereby releasing heat). In Auger recombination, an excited electron experiences a scattering event with another excited state electron, transferring its energy. The first electron falls back to the ground state having given up its energy, and the second electron is excited to an even higher state. This electron can then thermally relax back to the edge of the conduction band in an overall trimolecular process. Given the order of these processes, as the number of charge carriers increases, higher order recombination processes become more probable. In the double perovskites studied in this work, there was no evidence of Auger recombination. TRMC measurements allow for the recombination behavior of charge carriers over time to be observed. This allows for an identification of the dominant loss mechanisms in the film, and provides a clearer picture of what the defects in the material are.

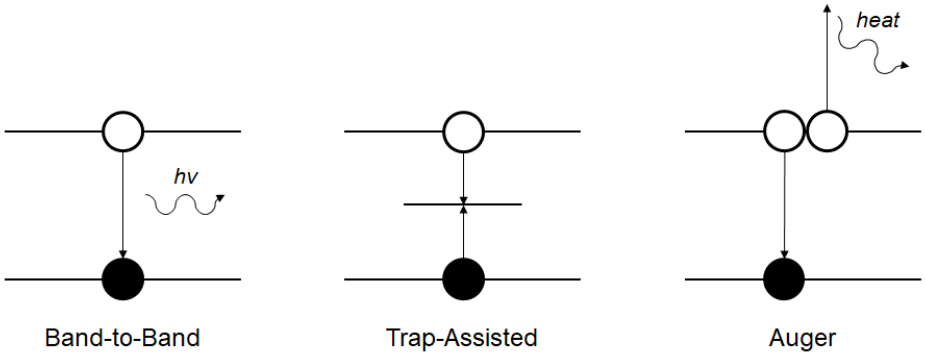

Figure 2.2: A simplified diagram showing potential pathways for charge carrier recombination, with the conduction band and valence band represented by horizontal lines on top and bottom, respectively.

Direct and Indirect Semiconductors

Band theory is an extension of MO Theory for a crystal lattice, and as such, is based on approximate solutions to the wavefunction. Solutions for the energy of the one-dimensional wavefunction lead to an energy dependence on a so-called wavenumber k, a value which can be thought of as a spatial reciprocal of the wavelength. As the system is extended to higher dimensions, the wavenumber becomes a wavevector, describing the solution to the wavefunction in the x, y, and z dimensions. Given that the shapes of the s, p, d, and f orbitals are increasingly complex, and as different elements are incorporated in the semiconductor, the wavefunction and its solutions become more complex as well

[27]. In order to better represent the information of the complex band structure of a real semiconductor, a plot called a k-space plot is constructed. The set of all unique wavevectors form an irreducible representation known as the Brillouin zone, a reciprocal space directly related to the real-space of the lattice. Within the Brillouin Zone, a path is drawn between points of high symmetry, and the electronic band structure is plotted along this path as a function of the wavevector k (see Figure 2.3).

If the highest position of the valence band coincides with the same k-value of the lowest position of the conduction band, the material is said to be a direct semiconductor, requiring only the absorption of a photon of sufficient energy to excite an electron. If the maximal/minimal position of the valence/conduction band do not coincide at the same k-value, the material is said to be an indirect semiconductor, requiring both a photon of sufficient energy as well as a lattice vibration (phonon) to absorb the light and excite an electron. Electrons can interact with these phonons to produce scattering of light, but both the probability of vibrational modes appearing and the probability of scattering via electron-phonon coupling decrease with decreasing temperature [29, 30]. The current leading perovskite PV cells make use of direct band gap perovskites such as $CH_3NH_3PbI_3$, and consequently can use much thinner films than an indirect material (because direct band gap materials absorb light much better than indirect band gap materials). While $Cs_2AgBiBr_6$ is an indirect band gap material, it should not be excluded from the discussion of useful materials for PV devices. Silicon is an indirect semiconductor, but its technological maturity has allowed it to remain the dominant technology in the market.

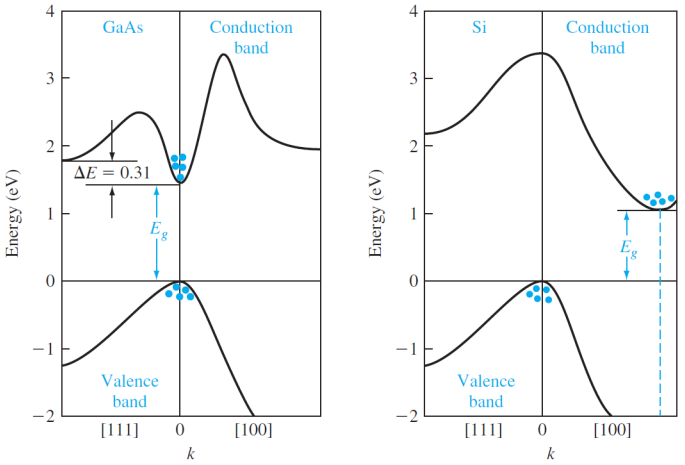

Figure 2.3: A diagram of the band edges for two industrially common semiconductors used for PV cells, gallium arsenide and silicon [27].

Excitons

The excitation of electrons to the conduction band does not always result in the formation of free charge carriers. Upon photoexcitation by light of energy just above the band gap, the excited electron is now electrostatically attracted to the newly created hole. If there is insufficient thermal energy to break this attraction (on the order of 0.01-1 eV), the electron and hole are spatially bound together by the electrostatic force and move as an electrically neutral quasiparticle called an exciton [31]. However, given their close physical proximity, the exciton tends to recombine quickly. Such a process is ideal for light emitting diodes (LED's), but detrimental for PV devices, as PV devices rely on the separation of charge carriers to drive a current.

There is considerable debate as to the nature of the peak that appears in the absorbance spectra of $Cs_2AgBiBr_6$. Some groups ascribe the peak to an excitonic transition in the material, but other groups ascribe it to an F-center (an anionic vacancy defect occupied by unpaired electrons) or other optical effect (scattering via electron-phonon coupling) [21, 32, 33]. Kentsch et al. measured the exciton binding energy of the silver-bismuth double perovskite to be 268 meV, approximately ten times higher than the thermal energy available at room temperature (k_BT = 25.9 meV) [32].

2.1.3. Perovskite Ionic Substitution

As mentioned in Chapter 1, the main compound studied in this thesis was $Cs_2AgBiBr_6$, a lead-free double perovskite. Double perovskites have chemical formulas $A_2B'B''X_6$, where B' and B'' are transition metal cations with charge 1+ and 3+, respectively. The choice of Ag^{1+} and Bi^{3+} to replace Pb^{2+} was not random, as only certain ions will satisfy the criteria needed to create a stable compound with the same structure via ion replacement (based on the size of the ions). The empirical criteria which govern whether an ion is of an appropriate size are known as the Goldschmidt Rules, and are expressed as follows [3]:

$$\mu = \frac{r_B}{r_X}, \quad 0.442 \leq \mu \leq 0.895 \qquad (2.1)$$

$$t = \frac{r_A + r_B}{\sqrt{2}(r_B + r_X)}, \quad 0.457 \leq t \leq 0.8553 \qquad (2.2)$$

where μ is the octahedral factor, r is the ionic radius, t is the tolerance factor, and A,B,and X indicate the ion in the perovskite chemical formula. The octahedral factor, μ, is a measure of the stability of the BX_6 octahedra, and values between 0.442 and 0.895 indicate stable octahedra. Tolerance factor values (t) less than 0.8 or greater than 1.0 indicate that the A site cation is too small or large, respectively, for a stable perovskite structure. A value of t between 0.8 and 0.89 indicates a distorted perovskite structure, and a value between 0.9 and 1.0 indicates a majority structure of standard cubic phase perovskite. For double perovskites, Equations 2.1 and 2.2 were modified by replacing r_B with the average ionic radii of B' and B". Table 2.1 shows the the calculated values of μ and t for $Cs_2AgBiBr_6$, $Cs_2AgSbBr_6$, and Cs_2AgBiI_6, using ionic radii values from Shannon [34].

The results indicate that while $Cs_2AgBiBr_6$ is fully stable, $Cs_2AgSbBr_6$ would have unstable octahedra, leading to poor perovskite stability. This prediction agrees with current literature, which shows that Sb^{3+} substitution for Bi^{3+} is difficult to achieve. The iodide complex was calculated to illustrate that the Goldschmidt Rules alone do not determine whether a certain material will form a stable double perovskite. Cs_2AgBiI_6 has thus far been reportedly only been synthesized as a nanocrystal via halide substitution, and as an extremely unstable thin film [22, 35]. Calculations of the heat of formation of the iodide complex are usually just above or just below zero, indicating a compound that is not very stable, contrary to the results of Table 2.1 [36, 37].

Table 2.1: Goldschmidt Rules results for double perovskites.

Material	μ_{avg}	t_{avg}
$Cs_2AgBiBr_6$	0.556	0.890
$Cs_2AgSbBr_6$	0.407	0.931
Cs_2AgBiI_6	0.495	0.877

2.2. Computational Chemistry

2.2.1. Quantum Mechanical Foundation

The aim of computational chemistry is to model chemical systems as accurately and efficiently as possible, and there is often an inherent tradeoff between accurately capturing all of the information of a chemical system and expending computational effort and time to do so. The most accurate description of a chemical system is its quantum mechanical description, where the wavefunction of the system contains all necessary information. An example of this is the time-independent Schrodinger Equation, shown in Equation 2.3:

$$\hat{H}\Psi = \frac{-\hbar^2}{2m}\nabla^2\Psi = E\Psi \qquad (2.3)$$

where $\hat{H}$ is the Hamiltonian operator, Ψ is the wavefunction, $\hbar$ is the reduced Planck constant, m is the mass of the particle, ∇ is the gradient operator, and E is the energy of the system. The solutions of the time-independent Schrodinger Equation can only be solved analytically for a limited number of systems (after multiple simplifying assumptions)[1], those systems having fewer than three particles. The reason for this limitation is analogous to the three-body problem of classical physics, involving calculating the motions of the Earth, Moon, and Sun as they affect each other gravitationally in their orbits. In the quantum mechanical system, the system of equations can no longer be solved analytically once three particles are present due to the electrostatic interactions between electrons and the nucleus and between electrons and other electrons. The energies which cannot be calculated analytically are the exchange energy and correlation energies (together referred to as the XC energy). The correlation energy refers to the electrostatic interaction between all of the electrons in the system while the exchange energy refers to the purely quantum mechanical effect of multiple particles being indistinguishable (such as the electrons in a chemical system). It is these energies that must be computed computationally in order to predict physical properties of the system using DFT.

[1] These assumptions include the Born-Oppenheimer Approximation, that the mass of the nucleus is so much greater than that of the electron that the kinetic energy of the nucleus can be ignored.

2.2.2. Density Functional Theory

Rather than attempting to track every electron in the system and calculate the interactions between them, Density Functional Theory (DFT) describes the chemical system in question through the use of functionals (functions of functions) that describe the electron density over the system as a function of position. Paul Hohenberg and Walter Kohn showed that the electron density of the system correlates directly to the energy of the system, and so the computational goal of DFT is to find the electron density that minimizes the total system energy [38]. The central problem is that the “true” electron density functional that correctly describes the motion and energetics of all electrons in the system (to calculate the XC energy mentioned in Section 2.2.1) is not known, and therefore many different functionals have been created, each with their own purpose and underlying methodology. For example, the most basic functional is the local density approximation (LDA), which requires very low computational effort but has poor accuracy. A hybrid functional named Becke 3-Parameter Lee-Yang-Parr (B3LYP) is an extremely popular functional that combines empirical corrections to the exchange energy from a Hartree-Fock type calculation with DFT to produce a functional with a reasonable compromise between accuracy and computational effort. With the advance of computing power over the past few decades, DFT has become the primary computational chemistry tool, with other less accurate but often computationally inexpensive methods such as the Hartree-Fock method and the Universal Force Field method sometimes applied for much larger systems.

3

Methods

3.1. Computational Methods

3.1.1. Foundational Options

Program

The program used for calculations was Amsterdam Density Functional (ADF), a popular quantum chemistry package which includes a powerful graphical user interface, allowing newcomers to the field to properly run complex calculations on large chemical systems. The options selected for DFT calculations in this work are detailed in the following sections [39].

Basis Set

The basis set is the set of functions which transform the differential equations of DFT into algebraic equations that can be solved by a computer (generally as a matrix). The smallest basis set, Single Zeta (SZ) describes each atomic orbital by a single basis function, such that a boron atom (electronic configuration $1s^2 2s^2 2p^1$) would have its orbitals described by three basis functions ($1s$, $2s$, and $2p_x$). Larger basis sets such as Triple Zeta Polarized (TZP) represent each atomic orbital by three basis functions and add another five basis functions to represent the d-orbitals. As the size of basis sets increases, both the computational accuracy and computational effort increase. In this work, the TZP basis set was selected for use in all calculations (justification provided in Section 3.1.3).

Exchange Correlation Functional

The purpose of the functional in DFT is to describe as accurately as possible the XC energy. As mentioned in Section 2.2.2, different XC functionals are constructed to account for specific interactions. For example, BLYP is a Generalized Gradient Approximation, and is a very local functional (as in, fragments of the system are influenced most by their immediate surroundings). It is a popular functional for geometry optimization, but another functional called BLYP-D3 includes the Grimme dispersion correction, which is useful to model systems with conjugated double bonds and π-stacked orbitals. In this work, BLYP was used for geometry optimizations and the long-range corrected functional CAM-B3LYP was used for simulations of the absorbance spectra (justification provided in Section 3.1.3).

3.1.2. Secondary Options

COSMO

As described thus far, DFT calculations of chemical systems treat the molecules as isolated, gas-phase systems in a vacuum. One way to model solution-based systems is to use molecular dynamics, which is a lower effort computational method that allows for modeling hundreds of explicit solvent molecules in a system. Another method within DFT is to use an implicit solvation model, in addition to explicitly coordinated solvent molecules. The Conductor-Like Screening Model of solvation (COSMO) is a continuum approach to model ions in solutions. The COSMO model places the solute in a cavity surrounded by a dielectric medium with a dielectric constant equal to the desired solvent's dielectric constant.

Frozen Core

All DFT calculations are a trade-off between computational time and accuracy. Another method used to lower computational time is to apply a so-called frozen core. From MO theory, it is known that the majority of elemental and molecular properties such as bonding, geometries, and reactivities, can be predicted solely by the valence electrons of the atoms involved. The frozen core option runs the calculation with the inner shells of electrons of an atom orthogonal to the valence shell of electrons, separating the two. This speeds up computation by eliminating calculations of interactions between the core electrons (numerous for heavy elements) and the typically small number of valence shell electrons, without losing too much information regarding the molecular properties. Mathematically, the frozen cores are solutions of a large basis set, all-electron calculation on the isolated atom.

Relativistic Effects

As electrons revolve around the nucleus, they are constantly subjected to an electrostatic potential with the nucleus and with other electrons. A common trait of heavier elements is that, due to an interaction of the electron's spin, the electrostatic potentials are affected, manifesting as a splitting of spectral lines. This process is called spin-orbit coupling (SOC). SOC is especially common for heavier elements and has been shown to be an important feature in lead-based perovskites, thus warranting some form of its inclusion in the DFT model [40]. While an accurate SOC calculation option exists in ADF, it is computationally intensive. As a compromise to include some form of relativistic effects without the full SOC treatment, the scalar relativity option was used. The scalar option employs the Darwin correction and the mass-velocity correction, which correct the potential energy in the case of electron charge smearing and correct the electron kinetic energy in the case of relativistic mass-variation, respectively [41].

3.1.3. Further Calculations

Interaction Energy

The interaction energy of a system is defined as the energy released or required to bring the component fragments from isolated systems into a combined molecular complex. This description is called the uncorrected method, because in DFT calculations, there is an issue with the above description called the Basis Set Superposition Error (BSSE). Each atom has its own basis functions, and when DFT calculations are run, those functions overlap in order to increase computational accuracy. However, this overlap (superposition of the basis sets) leads to an overestimation of the true interaction energy of the complex. To solve this, rather than comparing the energy of the isolated fragments versus the final molecule, a "ghosting" method is employed, whereby all atoms except the fragment in question are ghosted and the energy of the fragment is calculated. Ghosting treats the atom as though it has no electrons and no nuclei, but spatially preserves its basis functions. This allows for the energy of the fragment with interaction of the nearby basis functions to be properly calculated. The energy of all fragments with the rest of the molecule ghosted is then subtracted from the full complex energy to find the interaction energy. This method is called the corrected method, and the BSSE is defined as the difference between the corrected and uncorrected methods (see Figure 3.1).

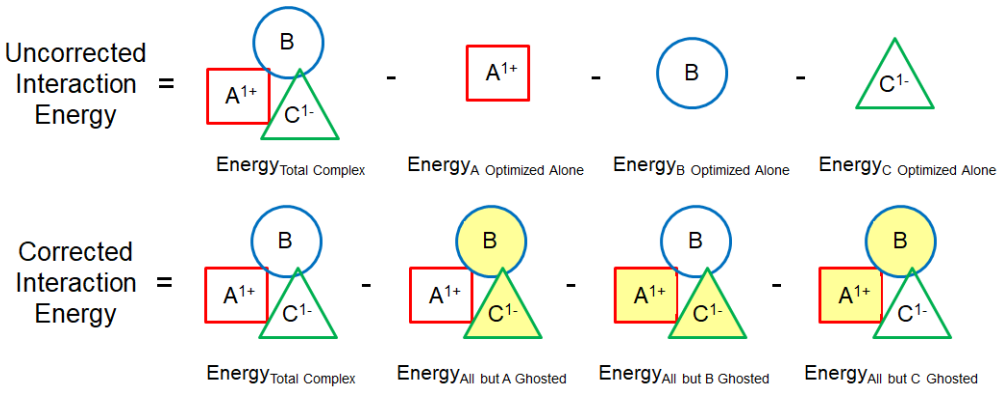

Figure 3.1: A diagram for interaction energy calculations involving 3 simplified species, A^{1+}, B, and C^{1-}.

However, as will be shown in Section 4.1.1, the ghosting method does not work in tandem with COSMO. It appears that the COSMO continuum shell is too large when attempting to analyze a central ion in a complex, thus reducing the effects of the dielectric continuum and incorrectly estimating the fragment energy of the central ion. Therefore, the calculations of the interaction energy were performed via the uncorrected method. While this indeed reintroduces the BSSE into the calculations, the relatively large basis set (TZP) significantly reduces the BSSE of the system to an acceptable level.

Time-Dependent Density Functional Theory

Time-Dependent Density Functional Theory (TD-DFT) is the computational method where solutions to the time-dependent Schrodinger Equation are solved. The method used in this work was the Davidson method. The Davidson method is a truncated form of the so-called Exact method, where each and every transition is calculated. As can be reasoned, calculating every excitation for every electronic transition of every ion in the entire complex would quickly become extremely computationally intense. In the Davidson method, the matrix from which the oscillator strengths and transition energies is obtained is diagonalized and only the lowest eigenvalues are calculated (theoretically corresponding to the lowest excitation energies and therefore most probable transitions).

The excitation of a molecule is essentially the molecule's response to an oscillating electric field (electromagnetic radiation). Upon excitation, the molecule is polarized, with electrons being drawn to a particular position based on the geometry of the system. While excitations are often thought of as a single electron rising in energy, the entire system undergoes a change, as each electron's position affects the positions of those around it, and it is important to capture this dynamic. As mentioned earlier, BLYP is a very local functional, and while sufficient for geometry optimizations, the longer range interactions that occur upon electronic excitation are better captured by a different functional, CAM-B3LYP (Coulomb-attenuating method Becke 3-Parameter Lee-Yang-Parr) [42]. CAM-B3LYP is a range-separated hybrid functional, combining different quantities of Hartree-Fock correction and Becke correction depending on whether the surrounding atoms are at short-range or long-range distances. With its emphasis on long-range interactions, CAM-B3LYP better approximates the excited state system.

3.2. Experimental Methods

3.2.1. Synthesis

Synthesis methods for the double perovskite $Cs_2AgBiBr_6$ are generally quite intensive, with procedures such as boiling precursors in 9M HBr (aq) or sintering precursor powders under vacuum for greater than 24 hours [19, 21, 43]. In this work, a simple synthesis was employed in a nitrogen-filled glovebox at positive pressure, similar to that of Hoye et al., Li et al., and Liu et al [25, 26, 44]. Precursor powders (CsBr, AgBr, $BiBr_3$, and $SbBr_3$) were added in stoichiometric amounts to dimethyl sulfoxide (DMSO) to create a solution of 0.5 M of total double perovskite precursors. The solution was magnetically stirred on a hotplate at ~75°C. Following complete dissolution (after approximately 1-2.5 hours) the solution was cooled, filtered through a 0.22 µm polytetrafluoroethylene filter to remove any microscopic solids, and spin coated. The spin coating procedure was to deposit 100 µL of solution onto a plasma cleaned quartz substrate and spin coat at 4000 rpm for 40 seconds. Once the program finished, the sample was annealed on a hot plate for 5 minutes and then cooled on a steel surface.

3.2.2. Structural Characterization

X-Ray Diffraction

X-ray Diffraction (XRD) is an experimental technique used to determine the crystal structure of a material by striking the sample with x-rays and measuring the angles at which a detectable signal is produced. Amorphous samples produce no signal in the XRD because they do not have long-range order, and samples with higher crystallinity are preferred for PV applications as they tend to have better optoelectronic properties. The mathematical basis of XRD is described by Bragg's Law, which states that XRD reflections can only be seen when Equation 3.1 is satisfied:

$$n\lambda = 2d_{hkl}\sin(\theta) \tag{3.1}$$

where n is a positive integer, λ is the wavelength of incoming x-ray radiation, d_{hkl} is the interplanar atomic spacing for a plane with Miller indices of (hkl), and θ is the angle at which the x-ray strikes the

sample (compared to the plane of the sample rather than the normal to the sample). The interplanar spacing, d_{hkl} can be calculated geometrically based on the crystal system, and for cubic systems is expressed as per Equation 3.2:

$$d_{hkl} = \frac{a}{\sqrt{h^2 + k^2 + l^2}} \tag{3.2}$$

where a is the lattice parameter of the system. In the case of a cubic system, such as $Cs_2AgBiBr_6$ double perovskite at room temperature, a is equal to the side length of the unit cell [15, 45].

The diffractometer used for the XRD measurements was a Bruker D8 Advance, set up in θ-θ, Bragg-Brentano geometry with Co-κα1 radiation of wavelength (λ=1.789 Å). Figure 3.2 shows the geometry of the XRD setup. The x-ray beam was first filtered to eliminate Co-κβ radiation and reduce Co-κα2 radiation, then sent through a collimator to ensure parallel x-rays, and finally sent through a polarizing grating and diffraction slit to ensure a unidirectional field of x-rays striking the samples. The Co-κα2 radiation peaks remaining after filtering from the source were combined with their corresponding Co-κα1 peaks automatically by the software to form one peak in the output. A varying divergence slit was used, which increases the size of the beam which hits the sample in an attempt to counteract the natural loss of intensity at higher diffraction angles observed from the equation for scattering amplitude [45].

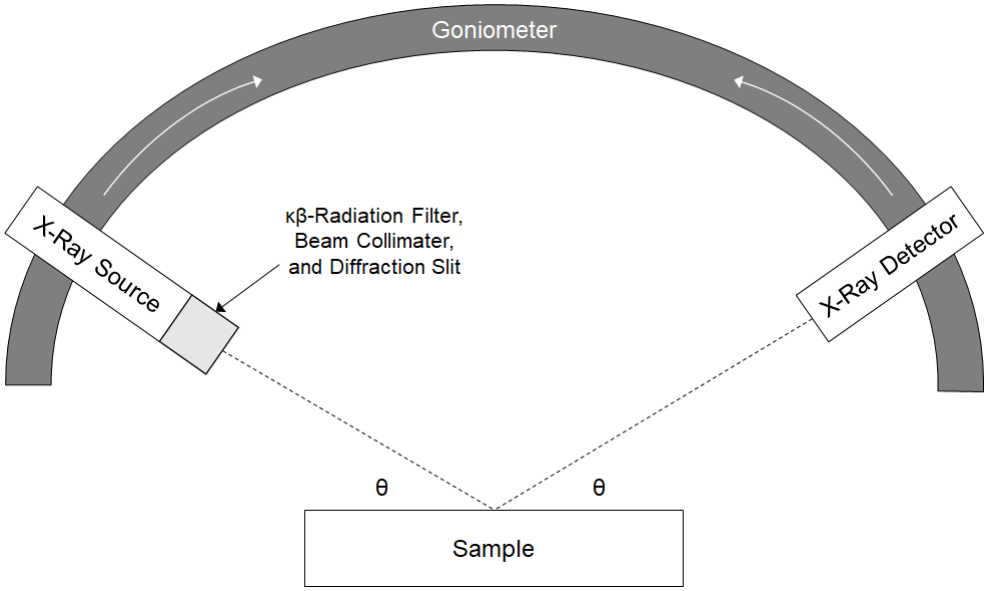

Figure 3.2: A simplified diagram showing the position of the x-ray source, x-ray detector, and sample. The goniometer moves the source and detector along the white arrows to sweep the specified ranges of 2θ.

θ-θ geometry is not ideal for the study of thin films, as the penetration depth of x-rays is typically greater than the thickness of the films, leading to a background noise of the underlying quartz substrate appearing in the XRD signal. However, the position of peaks remains constant, allowing for quick identification of the materials. The ideal geometry for thin film XRD analysis is the so-called grazing-incidence geometry, where the beam is kept essentially parallel to the sample to shine through the thin film material exclusively, with the detector sweeping around the sample. This method prevents quartz background noise from appearing in the signal, but requires significantly more time to set up for each sample, as the beam must be precisely focused into what is typically a <300 nm thickness film. Therefore, the more common θ-θ geometry was used.

Scanning Electron Microscopy and Energy Dispersive X-ray Spectroscopy

Scanning Electron Microscopy (SEM) is a powerful tool that allows visualization of materials at a resolution of 10's to 100's of nanometers. It operates by scanning the surface of the material with electrons of a specific energy. These electrons can either displace a valence electron from an atom on the surface, or be scattered by the electron cloud of the atoms. These electrons are detected separately to form a black and white image, with heavier elements tending to appear as brighter in the output because they

scatter electrons better than smaller atoms. One issue with SEM is that samples must be conductive. Without a conductive sample, the surface of the material will slowly charge with electrons over time, preventing data acquisition. To make sure the perovskite thin film would be conductive, it was spin coated on indium tin oxide (ITO), a conductive oxide often used as the n-type collector in perovskite PV cells.

Energy Dispersive X-ray Spectroscopy (EDXS) is a technique often built in to SEM machines used to analyze the composition of materials. Performed under the same conditions (high vacuum, conductive substrate, etc.), this technique involves striking the surface of the sample with electrons and ejecting a core electron, which produces an x-ray with a characteristic energy based on the element. These x-ray energies are matched to the characteristic x-ray energies to identify the elements present. This process is performed over a large area to obtain a map of the intensity of each element over the sample area. This information can be averaged to provide a quantitative measure of the amount of each element in a sample, providing information about the location of each element and the relative overall composition. In this work, the elements checked via EDXS were cesium, silver, bismuth, bromine, and antimony.

Profilometry

In order to determine the thickness of the spin coated samples, a Veeco-Bruker Dektak 8 Stylus Profilometer with stylus diameter of 12.5 µm was used. The thin film samples were scratched away using a toothpick at three locations (either end of the sample and the center), revealing the quartz substrate below. The Dektak operates by applying a user-specified stylus force of 2 mg (consistent with softer organic materials) in a straight line over a time of 30 seconds. The stylus's path is set to move over a portion of the sample containing both the exposed quartz and the thin film, and the measured height difference and sample roughness are recorded. The measurement is taken a total of 7 times on each sample, and averaged to provide a value of film thickness across the full surface.

3.2.3. Optoelectronic Characterization

Optical Absorption

The instrument used to measure the absorbance of the materials was a PerkinElmer LAMBDA 1050 UV/Vis/NIR Spectrophotometer with integrating sphere, deuterium and tungsten halogen lamps, and Peltier-cooled PbS and InGaAs detectors [46]. The machine and lamp were allowed to warm up for at least 30 minutes before any measurements were made in order to stabilize any fluctuations in the lamp's output. Thin film samples were measured using the integrating sphere, as per Figure 3.3. A plain quartz substrate was first measured in the integrating sphere, and its contribution to the absorption of light was subtracted before calculations of the final absorbance.

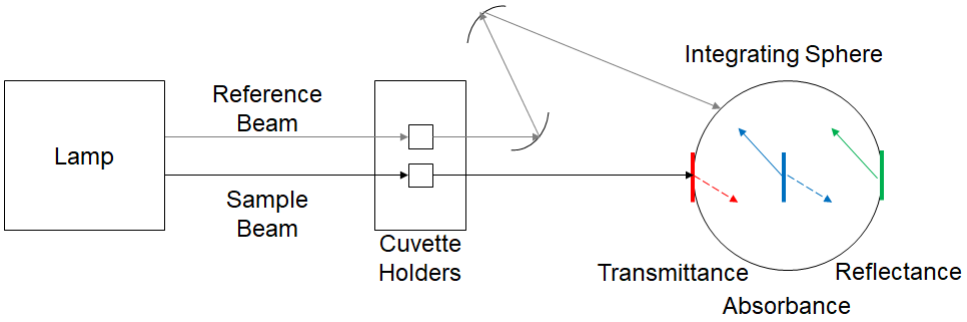

Figure 3.3: The diagram shows the capabilities of the spectrophotometer. The detector is located at the bottom of the integrating sphere, which collects light that enters the sphere. The thin film sample can be placed at either the red, blue, or green position to find the transmittance, absorbance, or reflectance of the sample, respectively. The solid and dashed arrows indicate reflected or transmitted light. The cuvette holders can be used simultaneously, with the upper holder used to automatically reference the measured sample, removing the effects of solvent and quartz cuvette.

Absorbance is defined in Equation 3.3 [45]:

$$A = -\log_{10} T = -\log_{10}\left(\frac{I}{I_0}\right) \tag{3.3}$$

where A is the absorbance, T is the transmittance, I is the intensity of light leaving the sample, and I_0 is the incident light intensity. Using the integrating sphere as described in Figure 3.3 with the sample placed in the "Absorbance" location means that the light reaching the detector will be the sum of reflected and transmitted light.

The fraction of absorbed light can then be calculated using Equation 3.4 and then combined with Equation 3.3 to calculate the absorbance,

$$F_A = 1 - F_R - F_T \tag{3.4}$$

where F_A is the fraction of light absorbed, F_R is the fraction of light reflected, and F_T is the fraction of light transmitted.

Absorption in thin films is described in Figure 3.4. Another useful set of values to find from absorbance measurements is the attenuation coefficient as a function of the wavelength, $\alpha(\lambda)$. The attenuation coefficient allows for the creation of a Tauc plot, which helps to determine the type of electronic transition occurring (direct/indirect, allowed/forbidden) [47].

A Tauc plot displays $(\alpha(\lambda) * E_{photon}(\lambda))^{1/r}$ on the ordinate and $E_{photon}(\lambda)$ on the abscissa, where the exponent $1/r$ determines the type of electronic transition occurring [47]. On a Tauc plot with the correct exponent, there should be a linear regime, which can be extrapolated to the x-axis to find the band gap of the material. For this work, r = 2.0 was used, indicating an indirect transition allowed by spin selection rules. To find the attenuation coefficient in thin films, the integrated form of Lambert's Law is used:

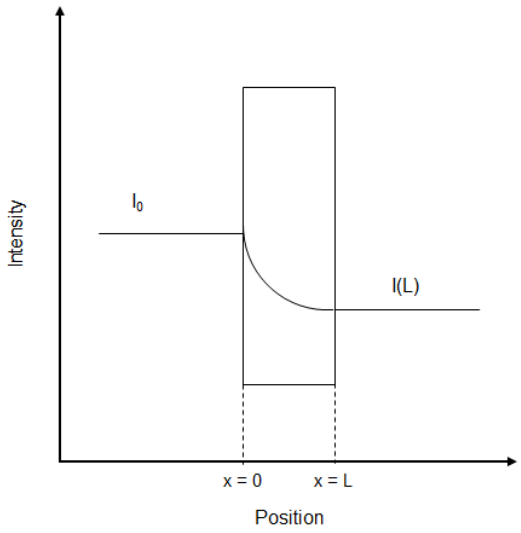

Figure 3.4: The diagram shows that as light passes through a material, its intensity decreases exponentially until it exits the material.

$$\frac{I(L)}{I_0} = e^{-\alpha(\lambda)L} \tag{3.5}$$

where L is the total film thickness, and using the boundary condition that $I = I_0$ at $x = 0$. Combining Equations 3.3 and 3.5 together yields the final equation which can be used to calculate the attenuation coefficient:

$$\alpha(\lambda) = \frac{2.303A}{L} \tag{3.6}$$

Time-Resolved Microwave Conductivity

Time-Resolved Microwave Conductivity (TRMC) is an analytical technique used to quantify the mobilities and lifetimes of charge carriers in semiconductors. TRMC has certain advantages over other optoelectronic characterization techniques. One is that the technique does not use electrodes to collect charges for a signal, as charge extraction can itself often be a barrier in the system. Another is that the presence of excited state electrons is directly observed. For example, photoluminescence techniques require that a photoexcited electron recombine radiatively in order to produce a signal, entirely missing information of excited state electrons that have recombined non-radiatively due to trap states or crystal defects. TRMC allows for observation of the excited state electrons and therefore captures the dynamics of the system after photoexcitation. Further analysis and parameter fitting can also reveal information about the dominant recombination mechanisms and rate constants associated with the charge carrier dynamics [48].

A laser at 10 Hz frequency is used to excite electrons from the valence band to the conduction band. This results in an increase in free charge carriers in thin films samples, which changes the sample's conductivity. The electric field component of a GHz-order microwave interacts with the free charge carriers and is used to measure the sample. The difference in conductivity between the sample

before and after excitation is measured as a function of time. The additional free charge carriers formed by photo-excitation absorb microwaves, and cause a reduction in microwave power that reaches the detector, as expressed in Equation 3.7:

$$\frac{\Delta P}{P} = -K\Delta G \tag{3.7}$$

where $\frac{\Delta P}{P}$ is the fractional change in microwave signal, K is a sensitivity factor (determined for a specific sample holder and microwave frequency), and ΔG is the photoconductance. The conductivity of the sample is defined in Equation 3.8 and the photoconductance is proportional to it:

$$\sigma = e(n_n\mu_n + n_p\mu_p) = en_0\Sigma\mu \propto \Delta G \tag{3.8}$$

where e is the electron charge, n_n and n_p are the concentrations of electrons and holes respectively, μ_n and μ_p are the mobilities of the electrons and holes respectively, n_0 is the total concentration of free charge carriers (both electrons and holes), and $\Sigma\mu$ is the sum of the mobilities of the charge carriers. Figure 3.5 shows a simplified diagram of the TRMC measurement process. The equations show that the effect of electrons and holes cannot be separated by this detection method, as both charge carriers increase the conductivity of the sample, and therefore influence microwave measurement and photoconductivity calculations of the sample.

The typical data output from a TRMC measurement (called a trace) shows an instantaneous increase in the photoconductivity of the sample followed by a decay to zero at a long enough time scale (typically between nanoseconds or microseconds, depending on the sample). To normalize the results, the ordinate is plotted as $\Delta G/\beta e I_0$ with overall units of mobility (cm^2/V•s), where β is a ratio of the sample dimensions (height over width), e is the electron charge, and I_0 is the incident laser light intensity. This quantity can be further normalized by F_A, which is the fraction of absorbed photons. The total quantity $\Delta G/\beta e I_0 F_A$ represents the fully corrected photoconductivity of the sample, while also accounting for reflection and transmission. The decay in photoconductivity as a function of time can be explored by varying the laser light intensity to produce a larger number of charge carriers in the sample, leading to increasingly higher order recombination processes.

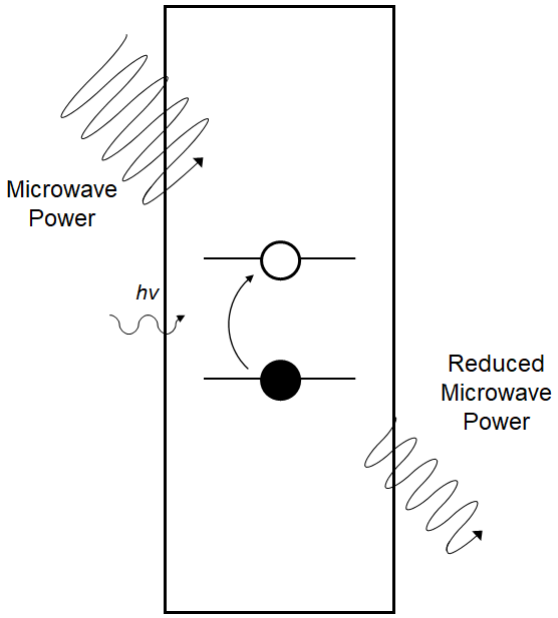

Figure 3.5: A simplified diagram of the core concept of TRMC measurements: the excitation of electrons and conductivity measurement via microwaves.

Samples are placed inside a gold plated sample holder closed with an iris. This iris allows microwaves to resonate and form a standing wave in the cavity of the sample holder before exiting to the detector, thus amplifying the signal. However, the rise time required to form the standing wave (18 ns) prevents full capture of the faster dynamics of the system compared to a sample holder without an iris (rise time of 3 ns) [49]. The sample with the cavity holder was required to amplify the signal as $Cs_2AgBiBr_6$, being an indirect band gap material, produces fewer free charge carriers with the same photon fluence compared to a direct band gap material.

4

Results and Discussion

4.1. Density Functional Theory

Attempting to dissolve individual precursors in DMSO led to the discovery that while CsBr, AgBr, and $BiBr_3$ dissolve together in DMSO, only $BiBr_3$ was individually soluble. When checking mixtures of $BiBr_3$ with the other precursors, $BiBr_3$ dissolved with CsBr but not with AgBr. Furthermore, a spin coated solution of all three precursors was found by XRD to have the correct double perovskite structure without annealing, meaning that that double perovskite crystallites were likely present in solution. These observations led to the hypothesis that the formation of the double perovskite in solution followed the pathway of dissolution of $BiBr_3$, followed by adduction with CsBr, and followed finally by adduction with AgBr to produce the double perovskite crystallite. Given the seemingly sequential nature of this process, the first complex studied was $BiBr_3$ in DMSO.

4.1.1. $BiBr_3$ Geometry Study

Initial Tests – Geometry

The first step in performing calculations was to check the effects of various functionals and basis sets on the calculation results. $BiBr_3$ was selected as the test molecule as it is small enough to run calculations fairly quickly and is charge neutral. Table 4.1 shows the results of geometry optimizations of $BiBr_3$ with different functionals and basis sets.

Table 4.1: Baseline test results for $BiBr_3$.

	BLYP			BLYP-D3			B3LYP		
Basis Set	Bi-Br Bond Length (pm)	Br-Bi-Br Bond Angle (°)	Mulliken Charge Bi, Br	Bi-Br Bond Length (pm)	Br-Bi-Br Bond Angle (°)	Mulliken Charge Bi, Br	Bi-Br Bond Length (pm)	Br-Bi-Br Bond Angle (°)	Mulliken Charge Bi, Br
SZ	266.6	99.7	0.34,-0.11	266.4	99.1	0.34,-0.11	257.0	100.0	0.17,-0.06
DZ	277.4	101.6	0.80,-0.27	276.9	100.5	0.80,-0.27	266.8	100.3	0.84,-0.28
DZP	272.6	101.7	1.09,-0.36	272.1	100.7	1.09,-0.36	262.6	100.3	1.14,-0.38
TZP	272.3	101.8	1.12,-0.37	271.8	100.9	1.12,-0.37	263.3	100.7	1.16,-0.39
TZ2P	270.2	101.2	0.96,-0.32	269.7	100.3	0.96,-0.32	261.2	100.2	1.14,-0.38
QZ4P	265.1	101.4	1.15,-0.38	264.8	100.6	1.15,-0.38	262.0	100.5	1.18,-0.39

There are small trends in bond lengths and Mulliken charges as the size of the basis set changes, with the geometry values converging after the SZ basis set and the Mulliken charges converging after the DZ basis set. One of the main results expected was that the Mulliken charge of the Bi^{3+} ion should be >1, as a heavy element can more easily accommodate a higher proportional partial charge. Basis sets above DZ tended to give this result, but the QZ4P basis set appeared to be too large to run computations in a reasonable time. The basis set TZP was thus selected as the largest basis set that provided accurate partial charges while requiring low computational effort.

Comparing between the different functionals, there was very little variation in the optimized geometry properties. However, B3LYP significantly increased computation time due to frozen core methods being incompatible with hybrid functionals, and the dispersion correction provided by BLYP-D3 appeared to do very little to change the computed geometry values. This left the lower-level GGA method BLYP as the functional of choice. The standard DFT options for the geometry optimizations were thus fixed as: BLYP functional, TZP basis set, scalar relativity, small frozen core, and COSMO solvation.

Optimized Geometries

Geometry optimization calculations were performed on the full set of possible Bi-Br-DMSO complexes, with a possible maximum of six total ligands connected to a central bismuth ion. Comparing the optimized geometries of the same species with and without COSMO, the COSMO solvation model appeared to bring ligands closer together, with smaller angles between ligands. In the cases of four and five coordinated species, the geometries would sometimes be altogether different, even though the initial input geometries were the same. Examples of different optimized geometries with and without COSMO include $[BiBr_5]^{2-}$, which changes geometry from trigonal bipyramidal to square planar, and $[BiBr_1DMSO_4]^{2+}$, which changes from square pyramidal with the bromine at the apex, to square pyramidal with DMSO at the apex (shown in Figure 4.1). However, once a coordination number of six was reached for the central bismuth ion, the geometries did not differ between optimizations with and without COSMO, suggesting that the effects of the COSMO model were not enough to overcome the steric interactions of a highly coordinated species.

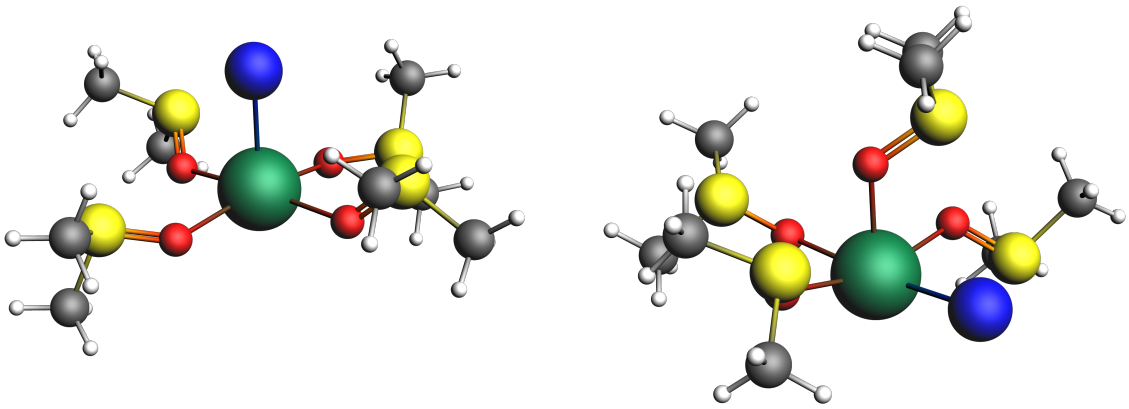

Figure 4.1: Optimized geometries of $[BiBr_1DMSO_4]^{2+}$ without COSMO (left) and with COSMO (right).

Interaction Energies of Bi-Br-DMSO Complexes

The interaction energies of the Bi-Br-DMSO complexes were calculated using the methods described in Section 3.1.3. The results of these calculations are presented in Figure 4.2, showing the results with and without COSMO, using both corrected and uncorrected methods. The figure should be examined vertically, with the values of the uncorrected interaction energy first, followed by the corrected interaction energy, followed by the difference between the two (the BSSE). The magnitudes of the interaction energy are significantly different between the calculations with and without COSMO, but that is to be expected given that COSMO has the effect of stabilizing individual ions (as does solvent in a solution).

From Figure 4.2, it is clear that the magnitude of the BSSE is much smaller without COSMO than with COSMO, as both the uncorrected and corrected interaction energies follow the same trend with similar energy values without COSMO. Figure 4.2e) indicates that there is an issue within the computational software when combining COSMO and the ghosting method required for the corrected interaction energy calculation. When examining the individual fragment energies, the Bi^{3+} ion was found to be the culprit (shown in Table A.1 in Appendix A). While DMSO and Br^{1-} have approximately the same energy as successive ligands are added to the complexes, the energy of the Bi^{3+} ion increases by ~2 eV as the number of ligands increases. As mentioned in Section 3.1.2, COSMO works by placing the molecule in a cavity surrounded by a dielectric continuum. The values in Table A.1 suggest that the effect of

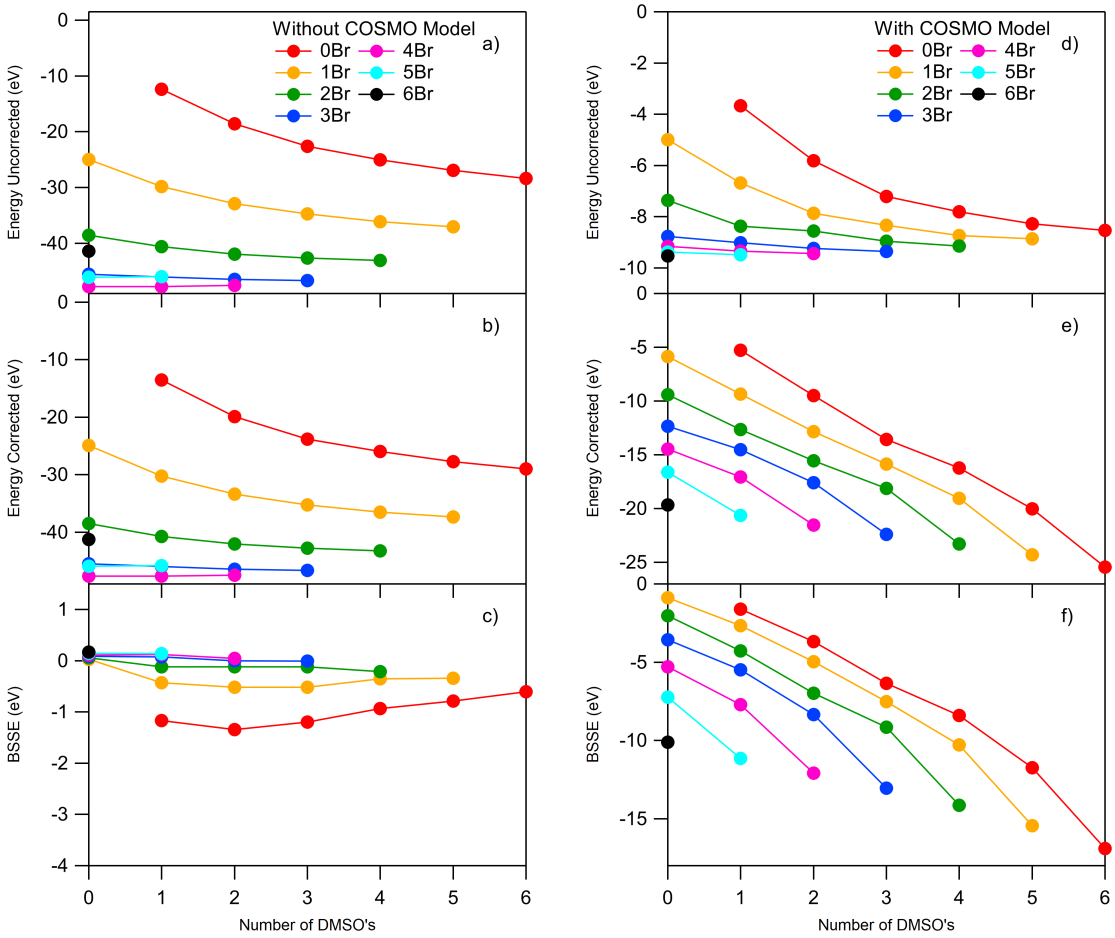

Figure 4.2: Plot of the Energies of the Bi-Br-DMSO complexes without COSMO (a, b, c) and with COSMO (d, e, f). a) and e) show the uncorrected interaction energy, b) and e) show the corrected interaction energy, and c) and f) show the BSSE difference.

COSMO diminishes as the ions are located further away from the surface of the cavity. With Bi^{3+} at the center of the cavity for higher coordinated complexes, COSMO may be having less of an effect on the ion, thus significantly changing the calculated energy of the ion and introducing large errors in the corrected method.

Because COSMO is needed to describe a chemical system in solution, the approach chosen was to proceed with COSMO, but to use the uncorrected interaction energy method, and accept a certain level of BSSE in the results. Figure 4.2c) shows that the magnitude of the BSSE is ~1 eV using basis set TZP on this system, and Figure 4.2d) shows that the interaction energies of the most stable complexes are ~ 9eV. This BSSE leads to an uncertainty of ~11% in the values of the interaction energy, which was deemed acceptable to proceed with the analysis.

4.1.2. Solution Spectroscopy – Experimental and Computational

Molecular Orbital Analysis

By examining Figure 4.2d), the most stable structures appear to be the six coordinated complexes with high numbers of bromine ligands. However, given the BSSE of ~1 eV, any of the highly coordinated complexes could potentially have very similar interaction energies. Therefore, the Bi-Br-DMSO complexes selected to be examined by TD-DFT were $[BiBr_6]^{3-}$, $[BiBr_3DMSO_3]$, and $[BiDMSO_6]^{3+}$, which provided a range between fully DMSO-bonded complexes and fully Br-bonded complexes. Figure 4.3 shows the typical molecular orbitals involved in the dominant simulated transitions of the Bi-Br-DMSO complexes.

The gold/brown and orange/cyan surfaces represent the positive/negative regions of molecular or-

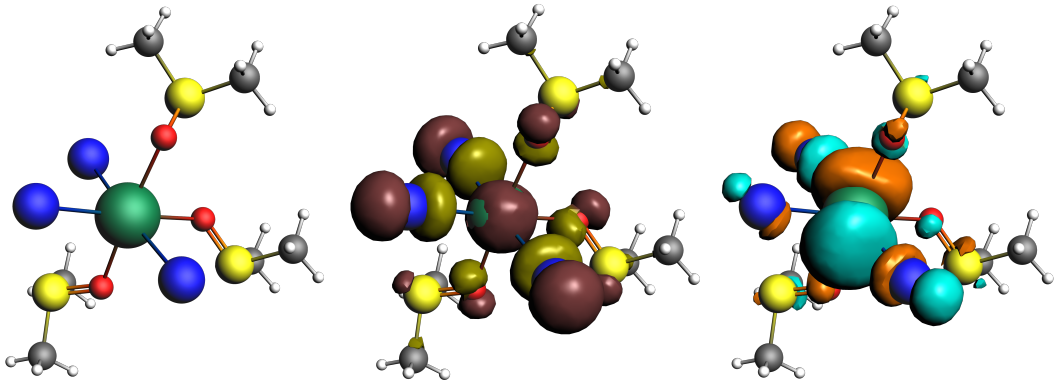

Figure 4.3: [$BiBr_3DMSO_3$] showing the optimized geometry (left), the HOMO showing mostly s-orbital character on the Bi^{3+} ion (center), and the LUMO showing mostly p-orbital character on the Bi^{3+} ion (right). Both HOMO and LUMO show p-orbital character on the Br^{1-} ions.

bitals and show the interactions across the molecule. In both HOMO and LUMO, the strongest interactions are between the central bismuth ion and the bromine ligands, with smaller contributions from the DMSO ligands. The HOMO shows the $6s$ orbital of bismuth interacting mainly with the $3p$ orbital of the bromines, while the LUMO shows the $5p$ orbital of the bismuth interacting mainly with the $3p$ orbital of the bromines. These observations are consistent with a charge transfer, in this case, a metal-to-ligand charge transfer. This description can also be visualized more clearly by examining the MO diagram of a $[BiBr_6]^{3-}$ complex (see Figure 4.4), which undergoes the same dominant transition. $[BiBr_6]^{3-}$ was used for the MO diagram, as its symmetry and simplicity make the MO diagram much easier to examine.

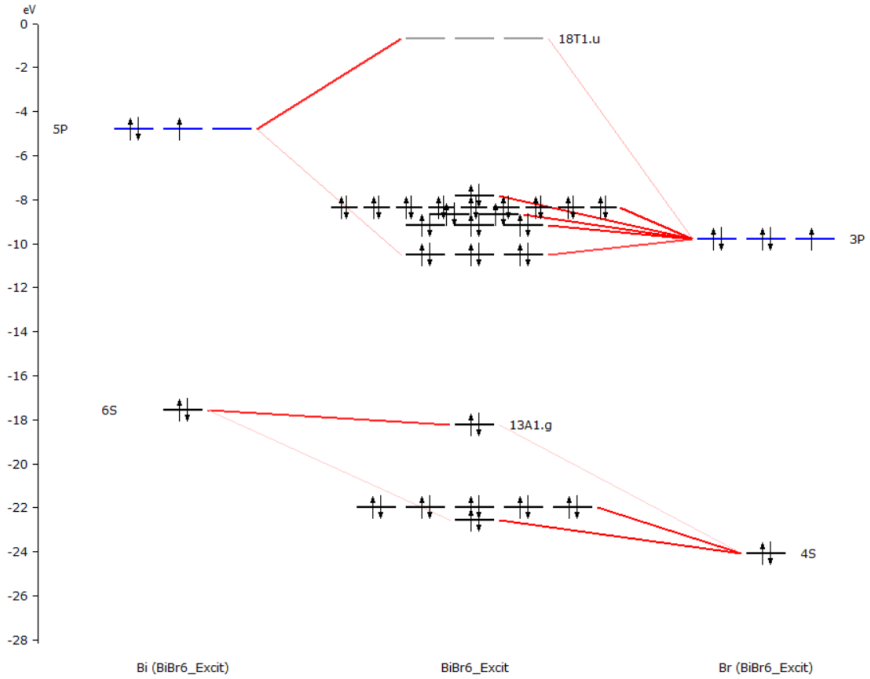

Figure 4.4: Molecular orbital diagram for $[BiBr_6]^{3-}$, showing a triply degenerate unoccupied state for the LUMO, with bismuth on the left and bromines on the right. The metal-to-ligand charge transfer involves an excitation from the 13_{a1g} MO to the 18_{t1u} MO.

Initial Tests – TD-DFT

With a new DFT calculation to perform (excitations rather than geometry optimizations), the choice of

functional must be re-examined. The simpler $[BiBr_6]^{3-}$ system was again examined, this time using BLYP, B3LYP, and CAM-B3LYP, with the simulated spectra shown in Figure 4.5.

There is a large shift of ~0.2 eV as successively longer-ranged functionals are used (BLYP to B3YLP to CAM-B3LYP). This shift is another indication that the electronic transition taking place is a charge transfer process. Given the difference in energies of the simulated spectra between the different functionals, it is clear that longer-range interactions are important in even the comparatively small $[BiBr_6]^{3-}$ system. Therefore, the functional which was specifically constructed to account for long-range interactions, CAM-B3LYP, was used for the TD-DFT calculations. The main DFT options for TD-DFT were thus fixed as: CAM-B3LYP functional, TZP basis set, scalar relativity, small frozen core,and COSMO solvation.

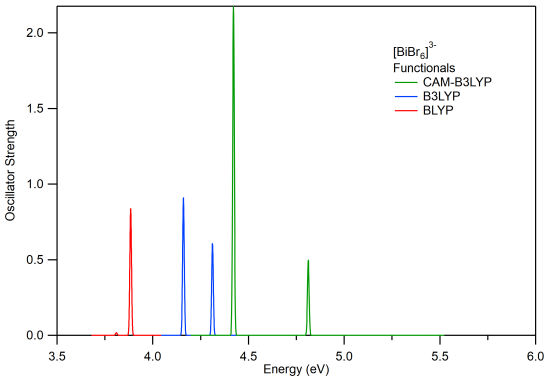

Figure 4.5: Plot of the simulated electronic transitions for $[BiBr_6]^{3-}$.

The other settings used were the precise calculation method for TD-DFT and the type of excitations. The method used was the Davidson method, which calculates only the lowest eigenvalues. Only singlet excitations were calculated, as the solutions displayed no observable phosphorescence, which would have indicated the presence of triplet states. Plots showing the effect of changing the calculation method, frozen core, and number of excitations are shown in Appendix Figures A.1 and A.2.

Experimental and Simulated Spectroscopy

The purpose of the DFT modeling was to determine what structures were present in solution. Therefore, UV-Vis spectroscopy on solutions was performed, beginning with $BiBr_3$ in DMSO. The concentration of solutions was initially set to 0.5 M in a 10 mm cuvette, resulting in absorbance measurements that were far too high to properly use. The solutions were eventually measured at a concentration of 0.5 mM, but even a 1000x reduction in concentration still had very high absorbance measurements, indicating the substantial absorbance of the complexes in solution. The experimental absorbance spectra of $BiBr_3$ solutions are shown in Figure 4.6a), where each solution had an overall concentration of 0.5 mM. Because absorbance is calculated on a logarithmic scale (see Equation 3.3), an absorbance value of 1, 2, or 3 indicate that 90%, 99%, or 99.9% of incident light was absorbed, respectively. In terms of instrumentation, this means that the detector is attempting to distinguish between extremely minute quantities of light, meaning that at high absorbances, the measurements must still be taken with some skepticism.

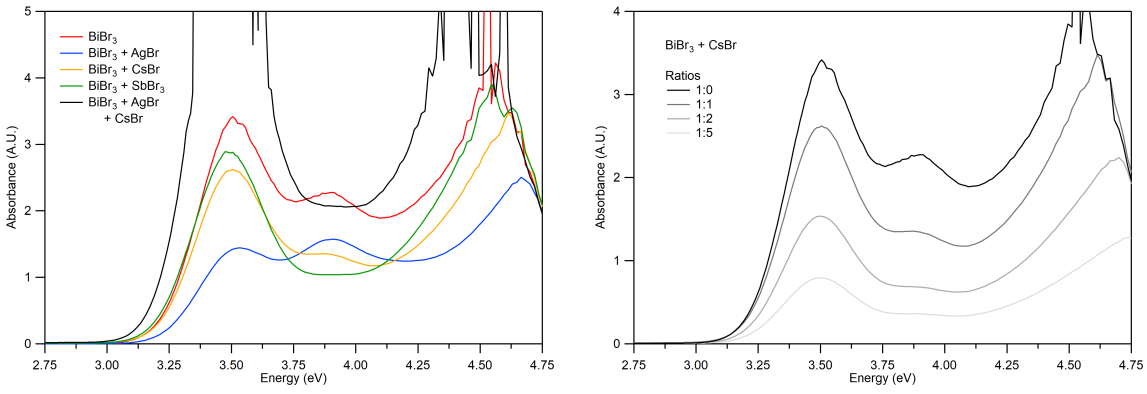

(a) $BiBr_3$ mixed with other precursors. **(b) $BiBr_3$ mixed with CsBr at different ratios.**

Figure 4.6: Experimental solution spectra, 0.5 mM, 10 mm cuvette.

Another feature of note that can be seen from Figure 4.6b) is that as the amount of CsBr in the solution increases, no new transitions are observed. However, the strength of the peaks of $BiBr_3$ (at 3.5

and 3.9 eV) is reduced. The lowering of $BiBr_3$ concentration in solution explains the decrease in peak strength and also helps explain the apparent “shift” of the peak at ~4.5 eV. The most likely explanation is that there is a very strong peak in the UV range, with a peak maximum somewhere between ~4.5-5.5 eV. As the concentration of $BiBr_3$ in solution reduces, the overall peak becomes smaller, leading to what appears to be a shift, which is in reality a peak size reduction. Lastly, the detector of the LAMBDA 1050 described in Section 3.2.3 has a minimum detection limit of 250 nm (4.95 eV). As such, it is possible that the detector signal has a larger scaling factor or higher error at energies just below 4.95 eV, leading to the apparent decrease in signals for high $BiBr_3$ ratio solutions.

Simulated Spectra of Bi-Br-DMSO Six–Coordinated Complexes

With similar interaction energies for all six-coordinated bismuth complexes, the simulated absorbance spectra were calculated using CAM-B3LYP for $[BiDMSO_6]^{3+}$, $[BiBr_3DMSO_3]$, and $[BiBr_6]^{3-}$. The results are shown in Figure 4.7. The visible trend is that as DMSO ligands are replaced by bromine ligands, the energy associated with the transitions becomes smaller. Comparing the results of Figure 4.7 to the experimental spectra of $BiBr_3$ in solution in Figure 4.6a), all of the simulated peaks are at energies higher than the experimental peaks at 3.5 and 3.9 eV.

This result indicates that larger complexes may be present in solution, as larger complexes tend to have lower absorption energies due to the band gap becoming smaller (see Figure 2.1).

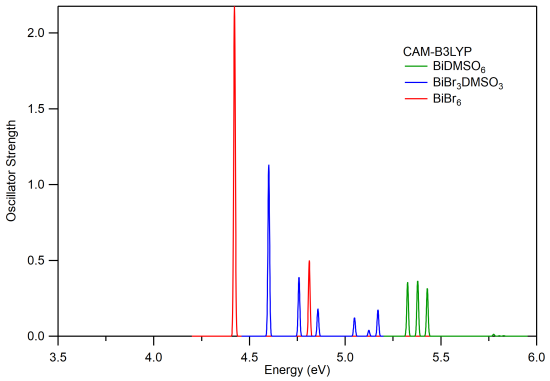

Figure 4.7: Six-coordinated Bi-Br-DMSO complexes.

Simulated Spectra of Larger Clusters of Bi-Br-DMSO and Cs–Complexed Clusters

The steps outlined for complexes containing a single bismuth ion were repeated for larger clusters of a Bi-Br-DMSO system containing more than one bismuth ion. The geometries were optimized using BLYP, and the simulated spectra of the optimized geometries were calculated using CAM-B3LYP. First, a single $[BiBr_6]^{3-}$ complex was tested with an increasing number of Cs^{1+} ions.

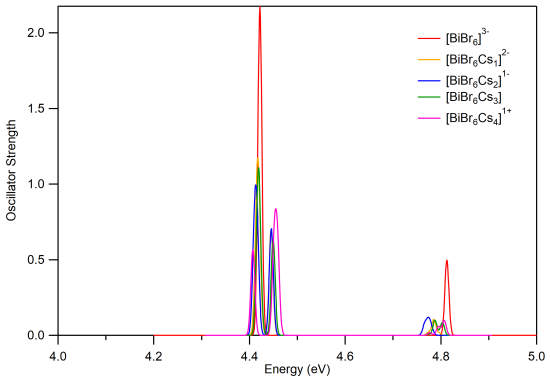

Figure 4.8: $[BiBr_6]^{3-}$ with Cs^{1+} ions.

Geometry optimizations resulted in the Cs^{1+} ions occupying the space where it would normally sit in the double perovskite bulk crystal. The simulated absorbance spectra are shown in Figure 4.8. The addition of Cs^{1+} ions results in very little change to the energies of the peaks, and only seems to cause some splitting of the lower peak at 4.4 eV. Examining the MO diagram, the energy of the MO’s arising from Cs^{1+} were above the MO’s of the metal-to-ligand charge transfer, thus not contributing to the simulated spectra. This result was consistent with experimental results showing no visible shift in peak energies.

Larger corner-sharing complexes with and without Cs^{1+} ions were also tested, with the results of their simulated absorbance spectra shown in Figures 4.9a) and 4.9b). Calculations of larger complexes both with and without Cs^{1+} ions converged, confirming numerical stability and at least indicating structural stability.

Figures 4.9a) and 4.9b) show a similar pattern for large clusters as Cs^{1+} ions are added as for the smaller $[BiBr_6]^{3-}$ cluster, namely a very small shift in energies with some spectral line splitting. The surprising result was that the peak energies did not monotonically decrease with cluster size. While $[Bi_4Br_{20}]^{8-}$ shows peaks that may match the experimental $BiBr_3$ solution spectrum peak at 3.9 eV, no complex was found to show peaks near 3.5 eV, the stronger experimental transition.

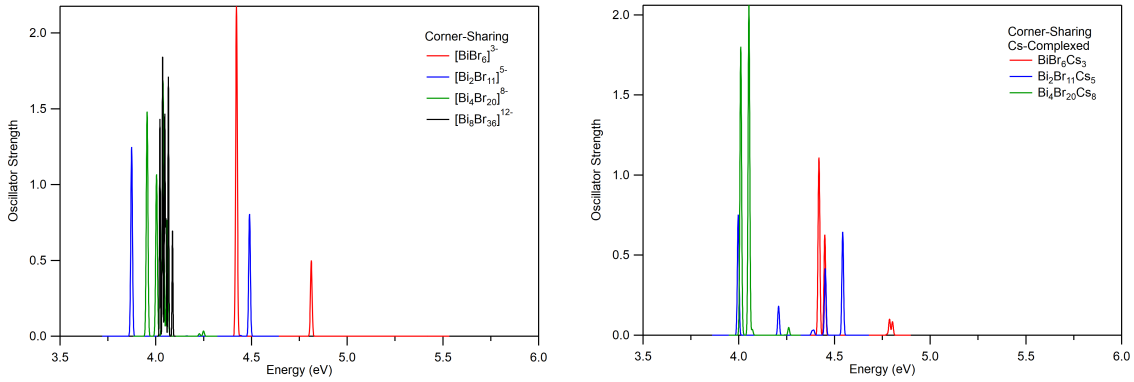

(a) Large clusters of $BiBr_3$. **(b) Large clusters of $BiBr_3$ with Cs^{1+} ions.**

Figure 4.9: Simulated absorbance spectra for larger complexes of $BiBr_3$ and complexes containing Cs^{1+}.

Further Analysis

The above analysis could be redone in an effort to find a more accurate answer. Due to the high absorbance of $BiBr_3$ solutions, a high dilution factor of 1000x was employed. This may have changed the majority species in solution by changing the equilibrium between the DMSO molecules and the complex. Additionally, the largest peak of the experimental absorbance spectra being located just beyond the range of the detector prevented peak position identification. These problems could be solved by using a spectrometer with a detector that is better tuned for absorption in the UV and by using an ultra-low path length cuvette (which are akin to microscope slides with a single drop of solution placed in between).The ultra-low path length cuvette should allow for solution spectroscopy without dilution. The effect of the functional was also noted to be substantial, with shifts of ~2 eV shown in Figure 4.5. Different functionals with different long-range interaction components could also be tested to see if the simulated spectra converge to a more precise range.

Further avenues of study include the dissolution $SbBr_3$ in DMSO and analysis of small fragments of double perovskite in solution. $SbBr_3$ was found to dissolve in a similar manner to $BiBr_3$, and a partial analysis of $SbBr_3$ in DMSO solution was performed similar to that done with $BiBr_3$, with the results shown in Figures A.3 and A.4. Additionally, combined solutions of CsBr, AgBr, $BiBr_3$, and $SbBr_3$ in varying Sb:Bi ratios were measured for their absorbance and an interesting pattern was seen, shown in Appendix Figure A.5.

4.2. Thin Film Analysis

4.2.1. $Cs_2AgBiBr_6$ – Structural Characterization

XRD and Absorbance Measurements

Synthesis of the spin coated double perovskite was performed at multiple annealing temperatures and confirmed by XRD to match the structure produced by Slavney et al. [15] The XRD diffractograms are shown in Figure 4.10.

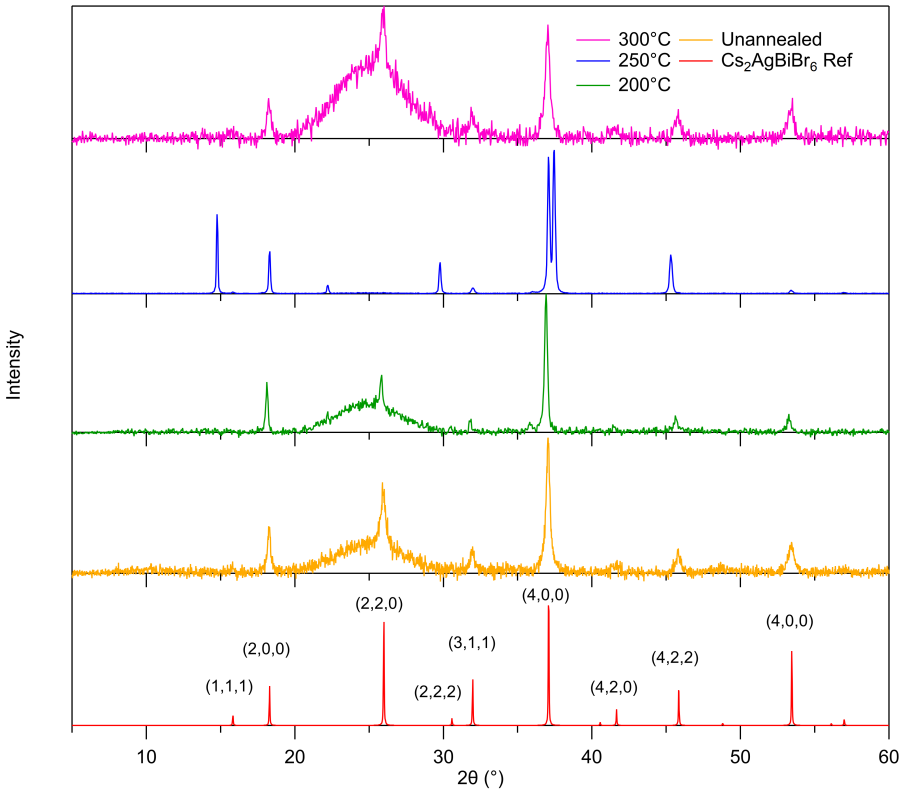

Figure 4.10: XRD of $Cs_2AgBiBr_6$ samples at multiple annealing temperatures with Miller indices referenced peaks.

The wide signal between 20-30° was a background signal resulting from the quartz substrate. The sample annealed at 250°C was seemingly far more crystalline in comparison to the unannealed sample and the samples annealed at 200°C and 300°C, and thus had a much higher signal-to-noise ratio, diminishing the quartz background noise. Given that peaks corresponding to reflections of multiple different lattice plane families appear, the sample is most likely a polycrystalline thin film, which is consistent with most spin coated thin films.

Further confirmation of the successful synthesis of the double perovskite came from UV-Vis absorbance measurements of the thin films. Figure 4.11 shows the absorbance of the same films. The absorbance spectra match those previously reported in literature, with a slow onset of absorption (the tail between ~2.0-2.5 eV), and a peak at ~2.8 eV (445 nm) [21]. The nature of the peak at ~2.8 eV is discussed later. The plots together demonstrate that the synthesis method described in Section 3.2.1 was successful in creating a polycrystalline sample of $Cs_2AgBiBr_6$, even without annealing.

Closer examination of the diffractogram of the sample annealed at 250°C revealed a double peak at $2\theta = 37°$, and extra peaks at $2\theta = 14°$ and 29°. Figure B.1 in Appendix B shows the diffractogram of this sample compared to common side products of the double perovskite synthesis, with the extra peaks ascribed to BiOBr impurity. More samples were synthesized, this time annealed at 240°C, 260°C, and 280°C, to hopefully find an optimal balance between high crystallinity and low BiOBr impurity formation. Figure 4.12 shows the diffractograms of these $Cs_2AgBiBr_6$ samples. There appeared to be an increase in the height of the BiOBr impurity phase as the annealing temperature increased. The sample annealed at 300°C in Figure 4.10 was expected to show considerable impurity, but may simply have had too low crystallinity to be able to resolve the BiOBr peaks.

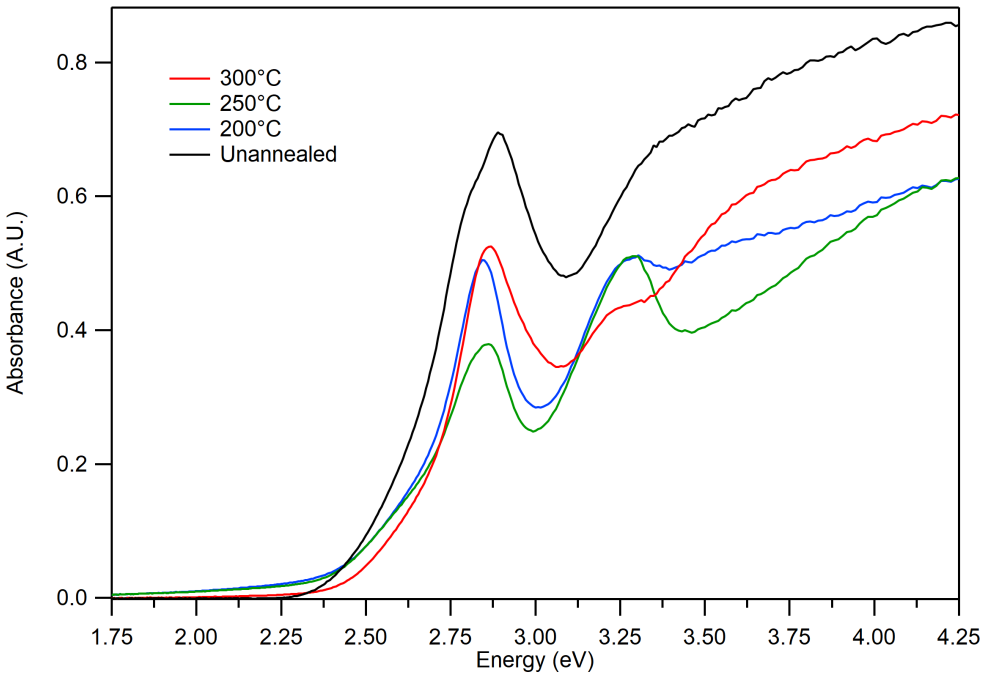

Figure 4.11: Absorbance measurements of $Cs_2AgBiBr_6$ samples annealed at high temperatures.

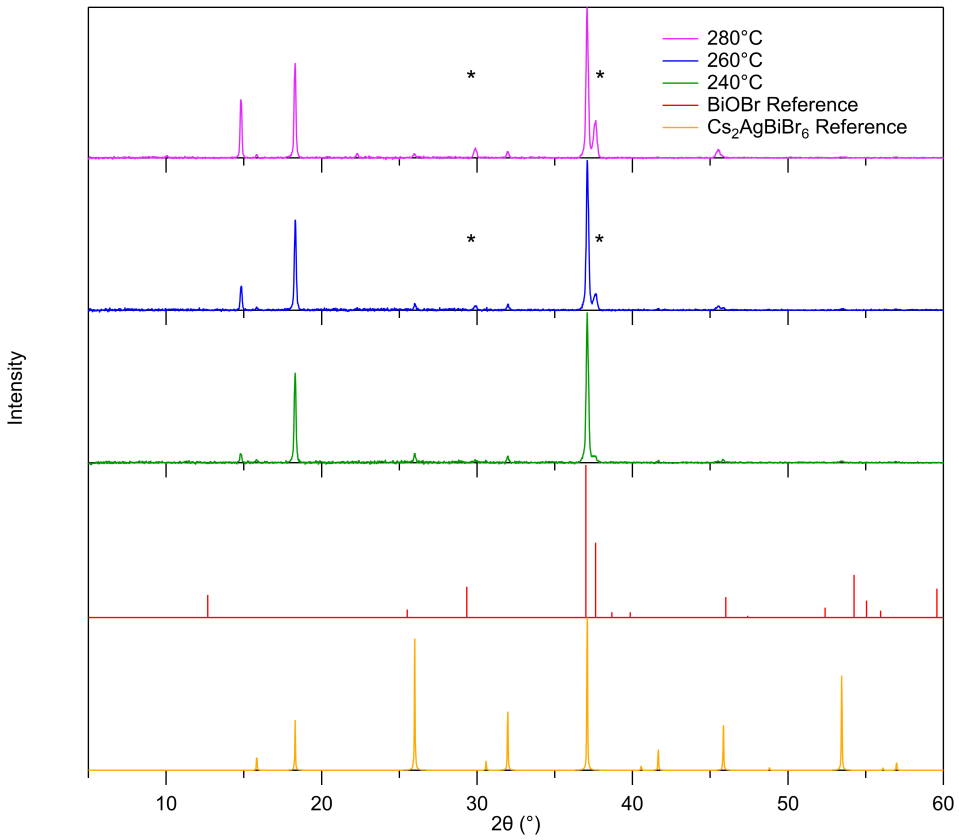

Figure 4.12: $Cs_2AgBiBr_6$ annealed at increasing temperatures showing an increase in BiOBr impurity.

Given that the entire synthesis had been performed in a nitrogen-filled glovebox above atmospheric pressure, the formation of an oxygen-containing side product was not very likely. The more likely scenario was that the material had degraded after exposure to air. To check this, another sample annealed at 250°C was synthesized, placed in an airtight XRD sample holder within the glovebox, and then analyzed via XRD without exposure to air. The sample holder was a plastic dome with a screw-down top and gasket on a non-XRD-reflective piece of polished silver. The results are shown in Figure 4.13. The outer plastic of the sample holder causes significant noise, but the peaks of the double perovskite are still visible in the correct positions, with no discernible degradation products.

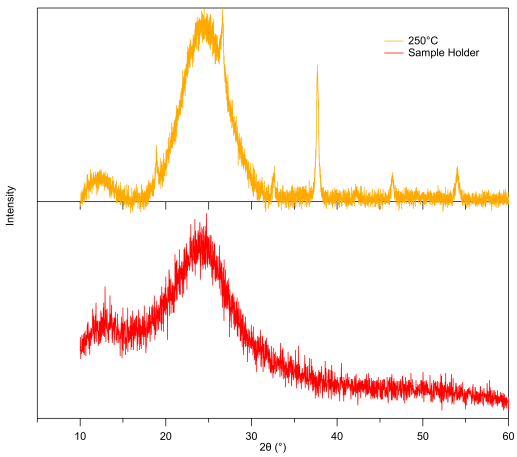

Figure 4.13: $Cs_2AgBiBr_6$ annealed at 250°C in an airtight holder, showing no BiOBr reflections.

SEM Imaging

SEM images were taken of two samples (see Figure 4.14), one annealed at 250°C and one at 90°C (to prevent side product formation [18]). The film annealed at 250°C had very small crystallites on the order of 100's of nanometers, with visible gaps of ~100 nm between the material. The film annealed at 90°C, on the other hand, had an extremely smooth and even surface coverage, which was hard to focus on and image given its smoothness.

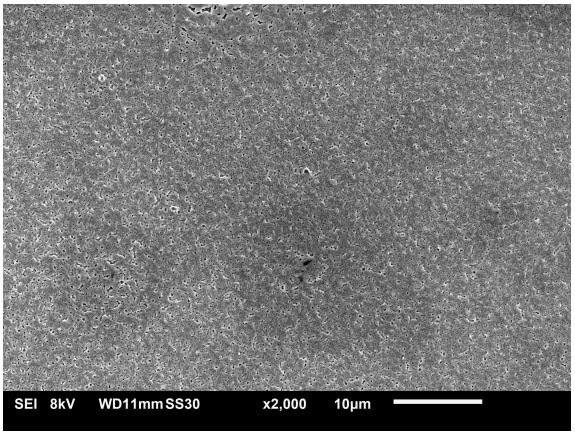

(a) Annealed at 250°C, 10 µm scale.

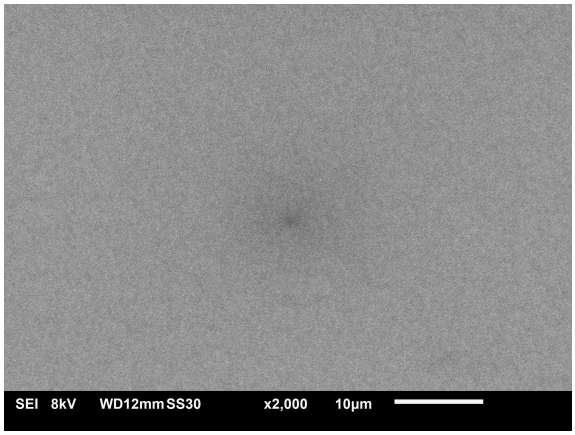

(b) Annealed at 90°C, 10 µm scale.

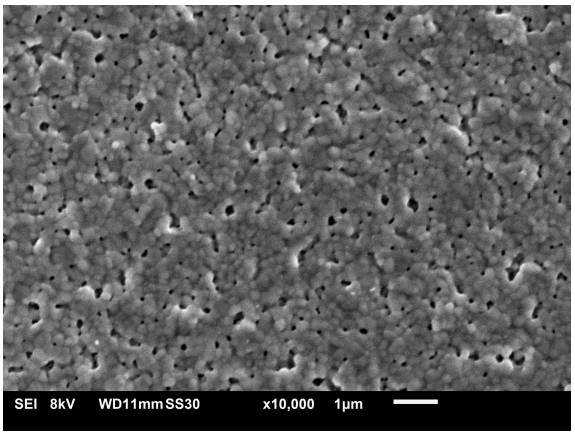

(c) Annealed at 250°C, 1 µm scale.

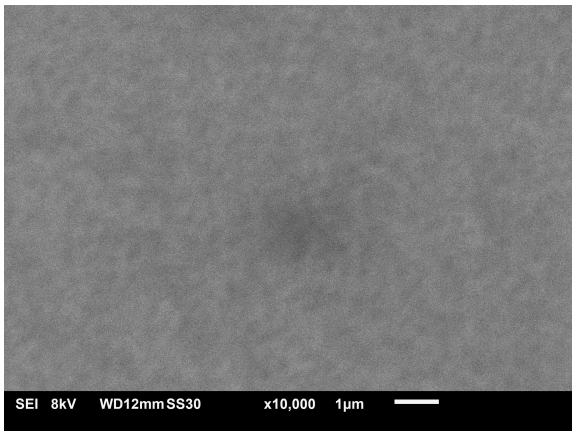

(d) Annealed at 90°C, 1 µm scale.

Figure 4.14: SEM images of the $Cs_2AgBiBr_6$ films annealed at different temperatures.

Given the difference in crystallinity observed from XRD measurements (comparing Figure 4.12 to Figure 4.20a)), the thin film annealed at 90°C was likely very amorphous, with higher temperatures necessary to provide enough thermal energy for the material to rearrange and crystallize. Slower, ramped annealing or an intermediate annealing temperature may result in the desired effect of achieving a sample of high crystallinity that is stable and resistant to degradation.

4.2.2. $Cs_2AgBiBr_6$ – Optoelectronic Characterization

Excitonic Transition

To probe the nature of the peak in the absorbance spectra, the sample was placed in a liquid helium-cooled cryostat, which allowed for precise temperature control, while simultaneously taking transmission measurements. The focus of the analysis was on the peak at 2.8 eV as that is where most of the difference in the spectra was expected (shown in Figure 4.15). The peak energy decreases until the sample temperature reaches 120°C, when it starts to increase again. This result is in agreement with the work of Schade et al. [50], who studied $Cs_2AgBiBr_6$ structure and optical properties with changing temperature, and found that the double perovskite undergoes a phase change at ~120°C from cubic to tetragonal. The shift in peak energies was found to follow proportionally to the tetragonal strain in the lattice.

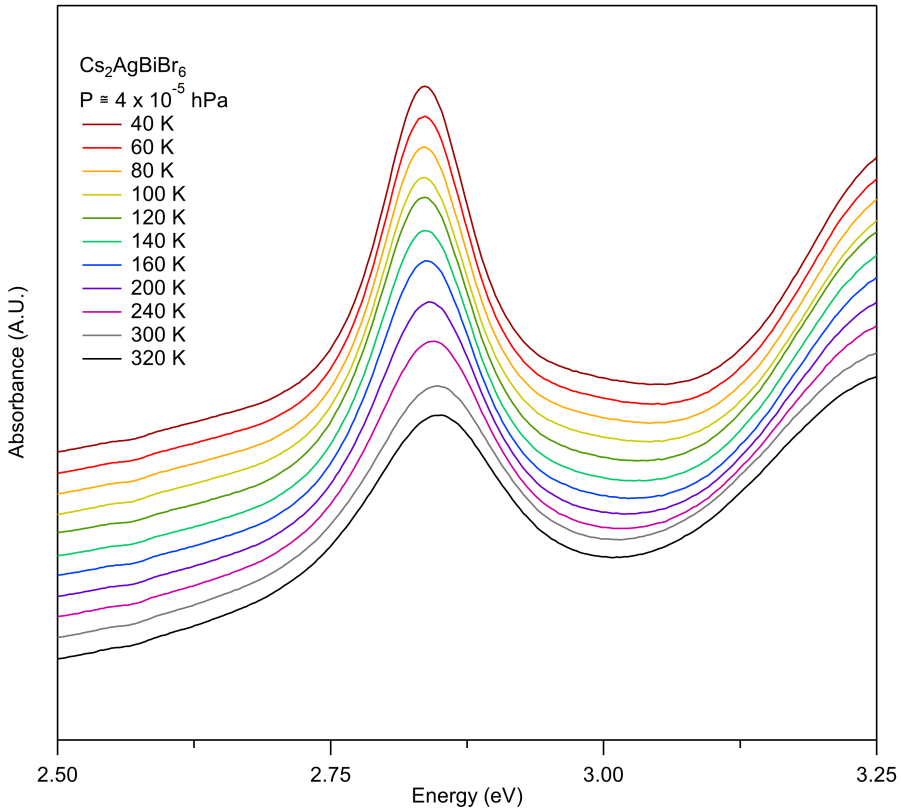

Figure 4.15: Absorbance spectra of $Cs_2AgBiBr_6$ at varying temperatures and fixed vacuum pressure. The individual measurements have been offset from each other to more clearly visualize the peak energy.

When the traces are viewed without offset (see Appendix Figure B.2), there is a noticeable increase in the peak height as the temperature decreases. This is inconsistent with the nature of the transition being due to scattering via electron-phonon coupling, as electron-phonon coupling increases at higher temperatures [29]. It is also intuitive that as the temperature increases, there are more vibrational modes of the ions in the lattice, leading to increased electron-phonon coupling. This intuition can be confirmed by examining the equation describing scattering probability via electron-phonon coupling, which scales as $e^{-1/kT}$ [30]. The shift in peak energy proportional to structural change and increase in peak height with decreasing temperature support the hypothesis that the peak is most likely the result of an excitonic transition rather than scattering via electron-phonon coupling, though this remains debated.

TRMC Measurements

TRMC measurements were performed on the $Cs_2AgBiBr_6$ samples annealed at various temperatures, at laser excitation wavelengths of 3.8 eV (325 nm), corrected by the fractional absorbance at the excitation energy. Performing TRMC measurements at this excitation energy allows for analysis well above the excitonic peak for an understanding of the charge transport properties of the thin film without too much interference from the excitonic contribution. To compare the effects of annealing temperature, a plot on a logarithmic scale showing a single trace from measurements of samples annealed at different temperatures was made (see Figure 4.16). There was an increase of two orders of magnitude in signal height as the annealing temperature increased, as well as a substantial increase in the charge carrier lifetime. This result was consistent with the observed difference in crystallinity from the XRD diffractograms of Figures 4.10, 4.12, and 4.20a), and the SEM images in Figure 4.14.

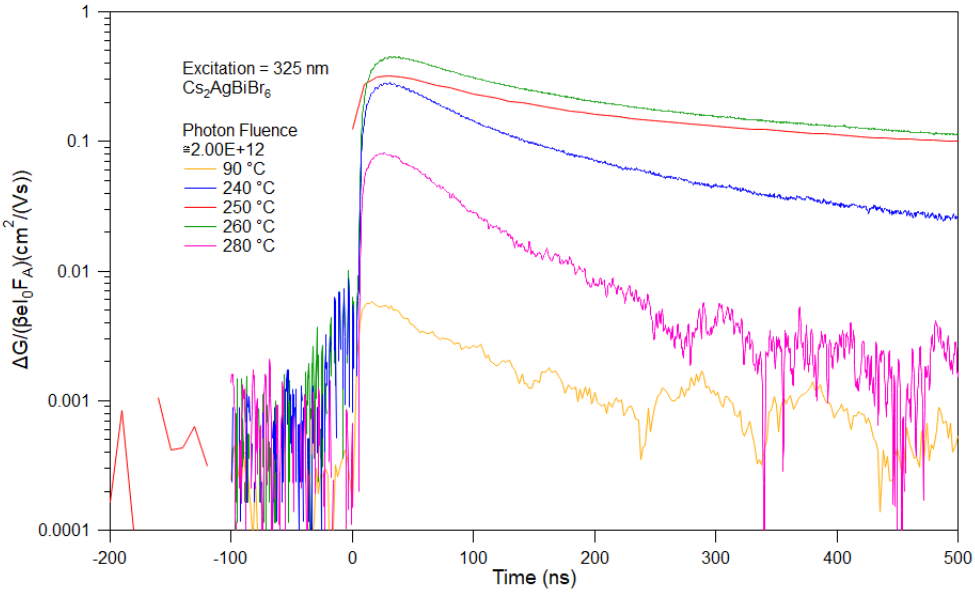

Figure 4.16: Plot of TRMC traces from measurements of multiple $Cs_2AgBiBr_6$ thin films with photon fluence $\cong 2 \times 10^{12}$.

For a more complete analysis, the full set of TRMC traces for the $Cs_2AgBiBr_6$ thin films annealed at 250°C and 90°C at laser excitation energies of 3.8 and 2.8 eV (325 and 445 nm), also corrected by the fractional absorbance, are shown in Figure 4.17. TRMC measurements were also performed at 2.35 eV (525 nm) in an attempt to measure optoelectronic properties near the band edge. However, correcting the TRMC traces by the fractional absorbance near the band edge proved inaccurate, as the absorbance is very low at that excitation energy. These plots have been included in Appendix B.

It is important to note the differences in the axes of both the time scale and the photoconductance in comparison of Figures 4.17a) and b) versus 4.17c) and d). As shown previously, the sample annealed at 250°C was more crystalline, and was therefore analyzed on a longer time window of 5 µs compared to the 1 µs window of the sample annealed at 90°C. The photon fluences used for the sample annealed at 250°C were also two orders of magnitude lower than the fluences used for the sample annealed at 90°C, and yielded maximum photoconductances that were two orders of magnitude higher.

From Figure 4.17a), the sample annealed at 250°C and excited at 3.8 eV, the behavior of a trap-filling regime was first observed as photon fluence increased. In the trap-filling regime, electrons are excited and immediately occupy trap states within the band gap. These trapped carriers cannot move freely, and thus do not contribute to the conductivity of the sample. As the photon fluence (and subsequently the concentration of charge carriers) increases, the maximum photoconductance of the sample increases, to a point. Eventually, the trap states are saturated by excited electrons and increasing the photon fluence results in free charge carriers rather than trapped electrons. As the photon fluence increases further, the decay of free charges becomes quicker due to an increase in recombination as the concentration of photoexcited electrons and holes increases. This results in both a faster decay of the TRMC traces and a lowering of the maximal value of the photoconductance. For the sample annealed at 90°C, the trap-filling regime was not observed, with only the decrease in normalized photoconductance

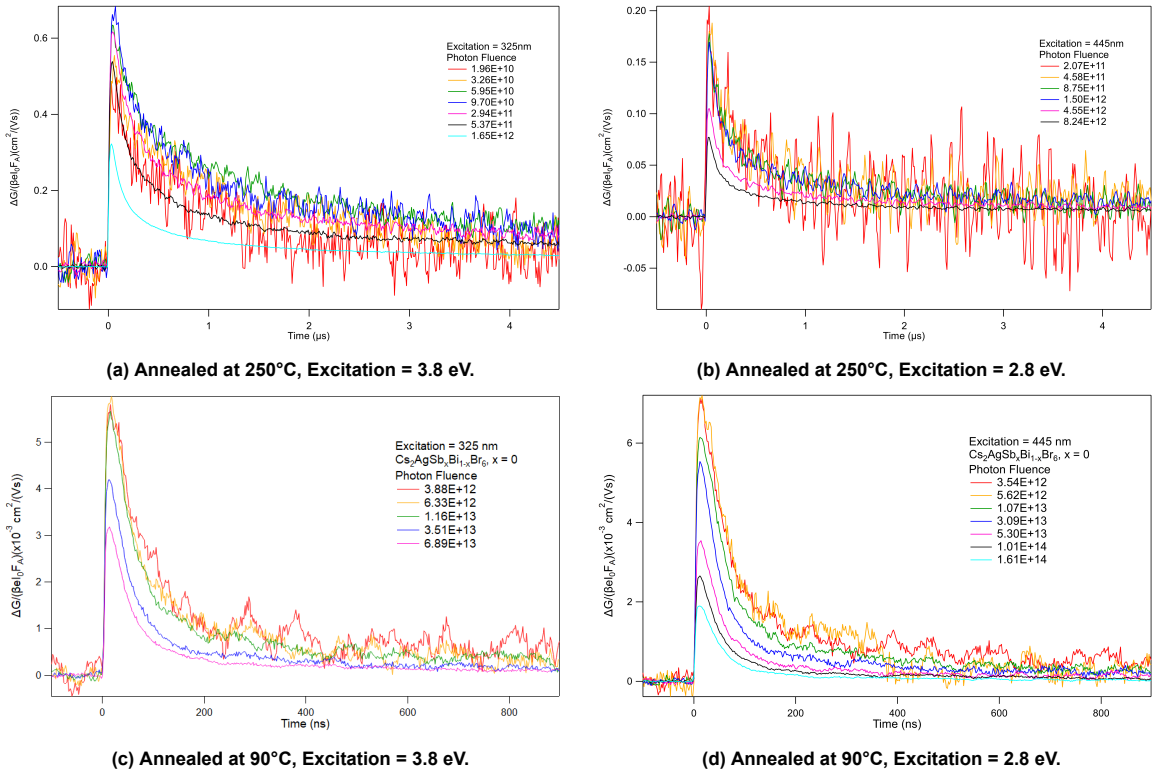

(a) Annealed at 250°C, Excitation = 3.8 eV.

(b) Annealed at 250°C, Excitation = 2.8 eV.

(c) Annealed at 90°C, Excitation = 3.8 eV.

(d) Annealed at 90°C, Excitation = 2.8 eV.

Figure 4.17: TRMC traces of $Cs_2AgBiBr_6$ thin films annealed at different temperatures, with thin films annealed at low temperatures plotted on different time and photoconductance scales.

observed with increasing photon fluence. The lack of trap-filling behavior for the samples annealed at 90°C was attributed to a a low signal to-noise ratio. Relatively high photon fluences of order 10^{12} were required to obtain an initial signal, meaning that the point at which all traps were saturated had likely already passed. This result, combined with the SEM images indicate that rather than discrete trap states present in a bulk crystal material, the photoexcited charge carriers were quickly recombining with dangling bonds between the semi-crystalline and amorphous regions via trap-assisted recombination, leading to a high signal-to-noise ratio. The amorphous phase explains the lower maximal photoconductance, as amorphous phase materials have a large proportion of dangling bonds, leading to distinct domains within the film. With low tunneling probability between these domains, the conductance of the sample after the excitation of electrons remains low, greatly diminishing the signal measured by conductivity measurements [51]. The decreased lifetime can be explained by charge carriers traveling a shorter distance before reaching a dangling bond and recombining, as opposed to travelling a longer distance to reach a point defect or grain boundary in the sample annealed at 250°C. The results of Figure 4.17 are consistent with literature reports for $Cs_2AgBiBr_6$ thin films annealed at temperatures $\geq$ 200°C and temperatures of 90°C, with a drop of 2-3 orders of magnitude in photoconductance signal.

There was also a significant decrease in the maximal photoconductance of the sample annealed at 250°C when excited at 3.8 eV versus 2.8 eV (factor of 1/3). This supported the hypothesis that the absorbance peak was the result of an excitonic transition, as excitons do not contribute to the conductivity of the sample. The sample annealed at 90°C surprisingly had a maximal photoconductance of similar values between the different excitation energies. However, this can again be explained by the amorphous nature of the film. While the absorption of light and formation of excitons is still possible, the conductivity of the sample does not significantly increase upon free charge generation nor upon exciton generation, thus maintaining the low signal level at each excitation energy.

4.2.3. $Cs_2AgSb_xBi_{1-x}Br_6$ – Structural Characterization

XRD and Absorbance Measurements

The possibility of ionic substitution of Sb^{3+} for Bi^{3+} was explored in an effort to make thin films with band

gaps more suitable for PV devices. Sb^{3+} substitution has been shown to reduce the band gap energy to a more favorable value for solar energy absorber materials, and its incorporation into $Cs_2AgSb_xBi_{1-x}Br_6$ via the facile synthesis method was tested. Figure 4.18 shows the diffractograms of the antimony substituted thin films annealed at 250°C. Side product formation was noted at x=0.4 and completely different crystal structures were observed for x=0.7 and x=1.0. The absorbance spectra for the proper double perovskite-structured samples is shown in Figure 4.19. Substitution of Sb^{3+} for Bi^{3+} should result in a decrease in lattice size and band gap, leading to XRD peaks appearing at larger angles and absorbance spectra with lower energy onsets. Close examination of the diffractograms for thin films annealed at 250°C indicated no substitution of Bi^{3+} for Sb^{3+} had occurred (with no shifts in XRD peak positions).

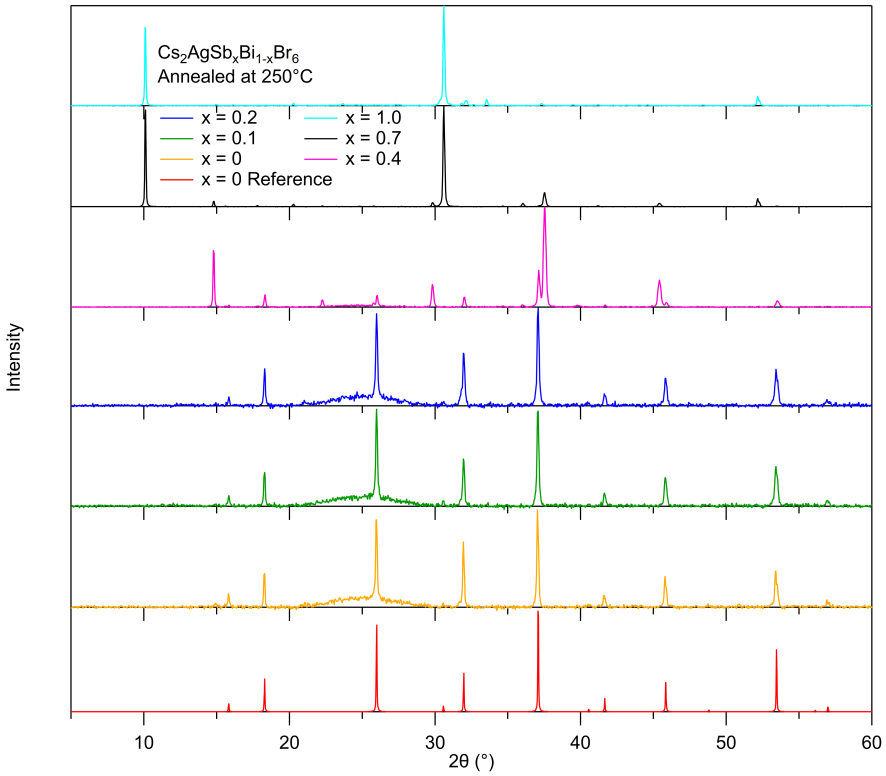

Figure 4.18: XRD diffractograms of $Cs_2AgSb_xBi_{1-x}Br_6$ thin films annealed at 250°C.

The absorbance spectra for the thin films annealed at 250°C showed some slight evidence of antimony substitution, with a small shift in the onset of absorption as the antimony content was increased. However, given that the diffractograms do not show any peak shifts to confirm this, it was concluded that thin films annealed at 250°C were not capable of antimony substitution.

Figure 4.20a) shows the full diffractograms of the antimony substituted thin films annealed at 90°C. The samples showed no side product or impurity formation except for x=1.0, and all samples appeared to have the correct double perovskite structure, though with lower crystallinity than samples annealed at 250°C. Figures 4.20b) and 4.20c) show zoomed in sections of Figure 4.20a) showing the peak shifts as smaller antimony ions replace larger bismuth ions in the lattice.

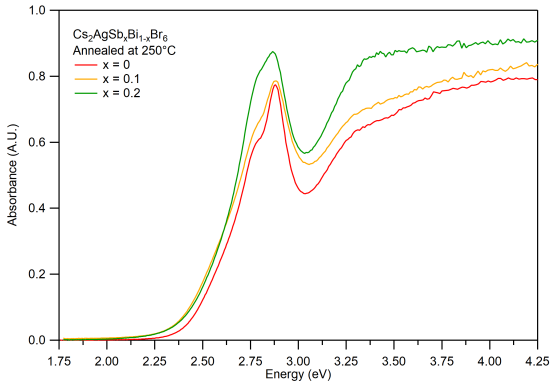

Figure 4.19: Absorbance spectra for $Cs_2AgSb_xBi_{1-x}Br_6$ thin films annealed at 250°C.

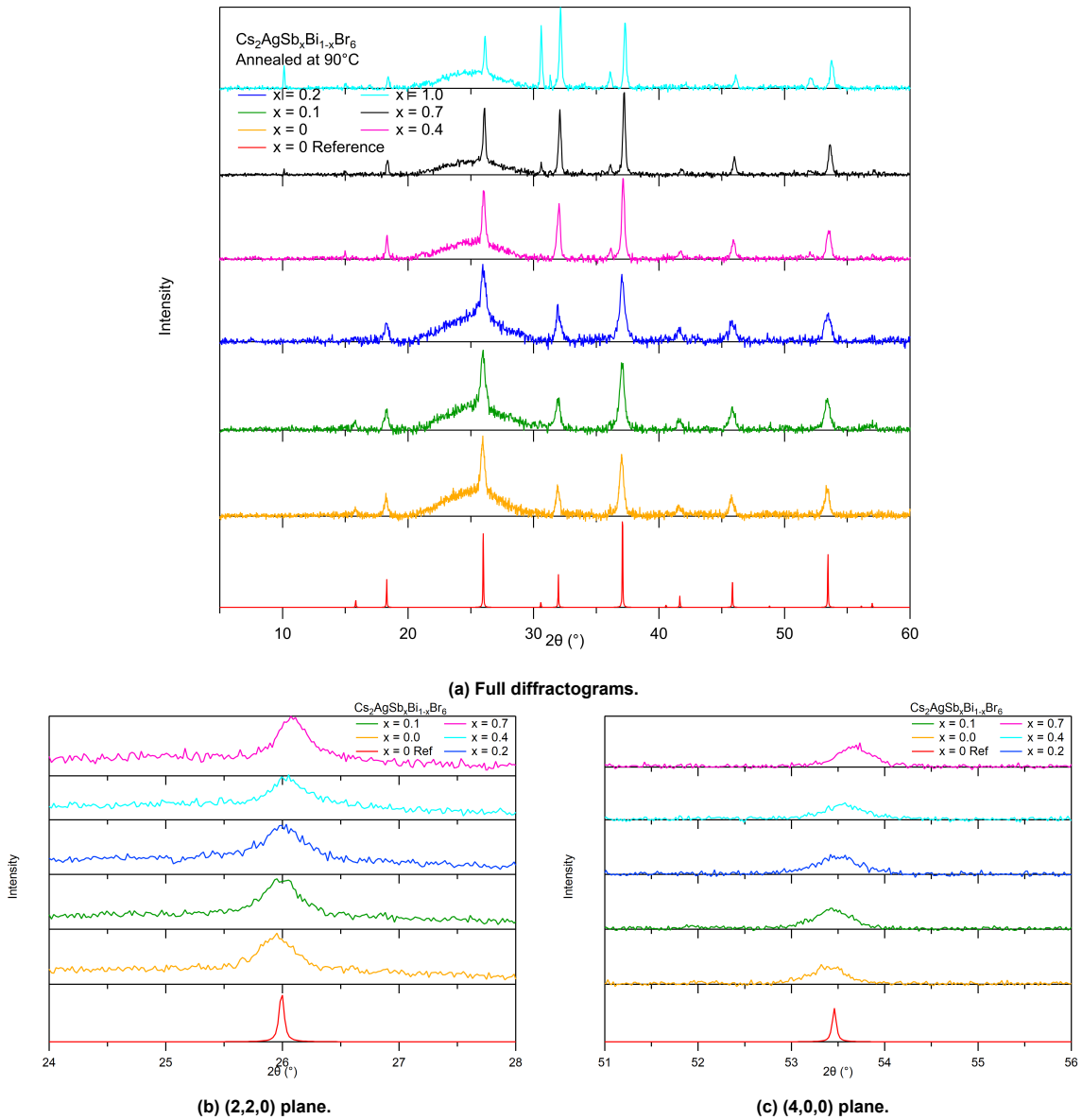

(a) Full diffractograms.

(b) (2,2,0) plane.

(c) (4,0,0) plane.

Figure 4.20: XRD Analysis of $Cs_2AgSb_xBi_{1-x}Br_6$ thin films annealed at 90°C.

The expected result was that the lattice parameter should decrease upon substitution of a smaller ion in the lattice, and this was confirmed by the calculations in Table 4.2, using Equations 3.1 and 3.2. The lattice parameter shifted by ~0.05 Å as the antimony content increased from x=0 to x=0.7. The ionic radii of six coordinated Sb^{3+} and Bi^{3+} are 0.76 Å and 1.03 Å, respectively [34]. While the lattice parameter shifts by a smaller amount than the difference in the ionic radii between Sb^{3+} and Bi^{3+}, this is to be expected, as other ions such as Br^{1-}, Cs^{1+}, and the remaining Bi^{3+} will keep the lattice closer to its original size.

The absorbance spectra for the double perovskite-structured samples with no impurities (x=0-0.7) are shown in Figure 4.21a), with the corresponding Tauc plots for an indirect, allowed transition (r = 2) shown in Figure 4.21b). Figure 4.22 is a photo of the thin films, showing a transition from yellow to orange with increasing antimony substitution, indicating a narrower band gap and earlier onset of absorption (consistent with the absorbance spectra).

Table 4.2: Shifts in the lattice parameter of $Cs_2AgSb_xBi_{1-x}Br_6$ upon increasing Sb^{3+} substitution, with a reported lattice parameter of 11.250 Å [15]. The difference calculated shifts between the two crystal planes may be a result of small sample height variations, which cause systematic shifts in peak positions across the diffractograms.

Crystal Plane	Sb^{3+} Content (x value)	Peak Position (°)	d_{hkl} (Å)	Lattice Parameter, a (Å)
(220)	0.0	25.95	4.088	11.564
	0.1	25.99	4.082	11.547
	0.2	26.01	4.080	11.539
	0.4	26.05	4.074	11.522
	0.7	26.08	4.069	11.510
				Total Shift = 0.054
(440)	0.0	53.40	2.228	12.606
	0.1	53.45	2.227	12.598
	0.2	53.50	2.226	12.589
	0.4	53.55	2.224	12.581
	0.7	53.68	2.220	12.560
				Total Shift = 0.045

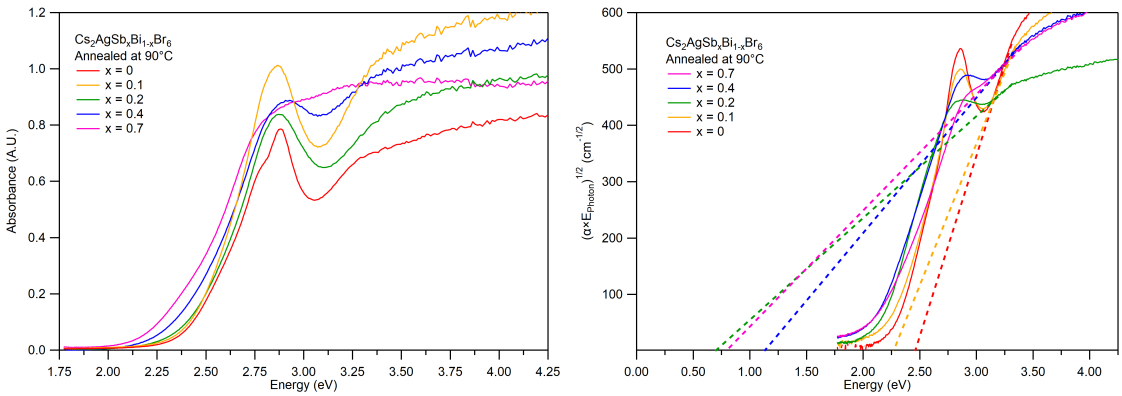

(a) Absorbance spectra showing the change in absorption onset and excitonic peak with increasing Sb^{3+} substitution.

(b) Tauc plots for indirect allowed transitions, with dashed lines indicating the linear regime extrapolated to the abscissa.

Figure 4.21: Absorbance analysis of $Cs_2AgSb_xBi_{1-x}Br_6$ thin films annealed at 90°C.

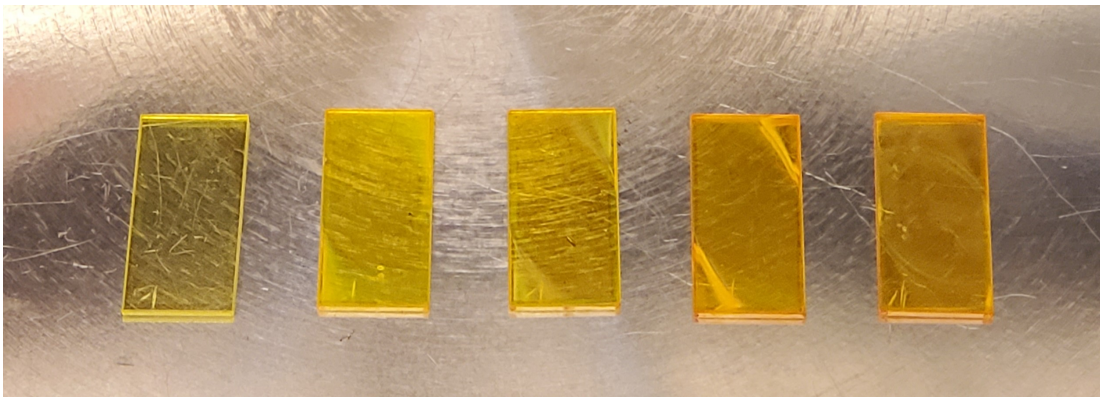

Figure 4.22: Photo of $Cs_2AgSb_xBi_{1-x}Br_6$ thin film samples. Left to right: x = 0, 0.1, 0.2, 0.4, 0.7.

Table 4.3 shows the calculated values of the band gap for an indirect, allowed transition (r = 2) with the attenuation coefficients found using the thicknesses in Appendix Table B.1. While the changes in diffractograms are consistent with Sb^{3+} substitution in the samples annealed at 90°C, the band gap energies calculated by the Tauc plots are not. The values of the band gap energies are as low as 0.75 eV, which is well below the energies for the indirect transitions of both $Cs_2AgBiBr_6$ (2.2 eV) and $Cs_2AgSbBr_6$ (2.08 eV) as found by DFT band structure calculations [25]. This was likely a result of the excitonic peak overlapping with the indirect transition, preventing an accurate assessment from being made via Tauc plot analysis. The onset of absorption does monotonicallly decrease as antimony substitution increases, which is consistent with both the expected results and reports in literature [18, 25].

The reason that lower temperatures incorporated antimony was not explored, but one hypothesis could be that annealing at high temperatures very quickly created silver-bismuth double perovskite crystallites. The formation of antimony-bromine octahedra may require longer times in a more amorphous system. A slower, ramped annealing method as mentioned earlier, or a two-step annealing method may be key to incorporating antimony while achieving a highly crystalline material with good optoelectronic properties.

Table 4.3: Band gap energies calculated from the slopes of the Tauc plot.

Sb^{3+} Content (x value)	Band Gap (eV)
0	2.47
0.1	2.26
0.2	0.72
0.4	1.15
0.7	0.80

Further confirmation of the Sb^{3+} substitution was attempted via EDXS, but the signal for antimony could not be detected. Samples analyzed via SEM were spin coated on ITO to improve conductivity for SEM imaging, but the large EDXS signal of the underlying tin overlapped with the smaller signal of antimony, preventing detection (see Appendix Figure B.3). EDXS could still be used in the future to confirm the presence of antimony, provided that the underlying conductive layer have a characteristic x-ray pattern with peaks far away from the rest of the elements in the sample (Cs, Ag, Bi, Sb, and Br).

4.2.4. $Cs_2AgSb_xBi_{1-x}Br_6$ – Optoelectronic Characterization

TRMC Measurements

In order to more easily compare the optoelectronic properties of the antimony substituted samples, combined TRMC plots were made. These plots (Figure 4.23), show a single TRMC trace from each sample (photon fluence $\cong 6 \times 10^{12}$) at an excitation energy of 3.8 eV (325 nm). The samples annealed at 90°C are all in the same relative range of photoconductance, as seen in Figure 4.23a). Figure 4.23b), however, also shows a trace from a sample annealed at 250°C, and shows the significance of the annealing temperature on the optoelectronic properties of the thin films.

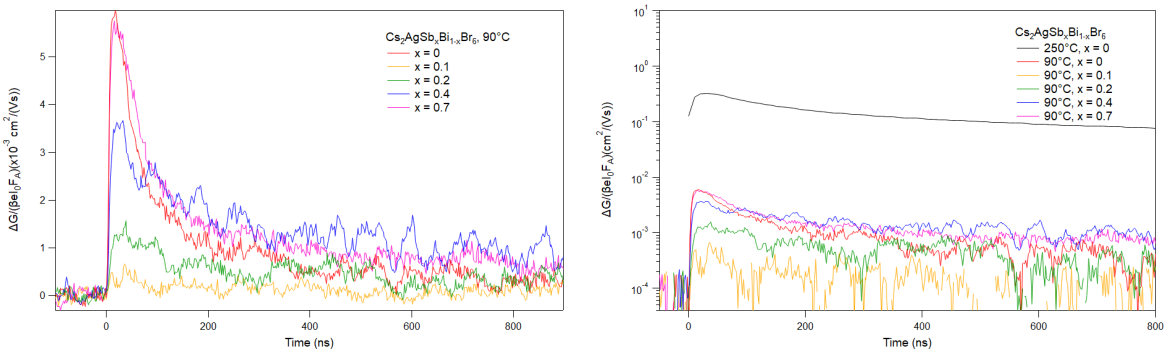

(a) Only films annealed at 90°C.

(b) Including a film annealed at 250°C on a log scale.

Figure 4.23: Plot of TRMC traces from measurements of multiple $Cs_2AgSb_xBi_{1-x}Br_6$ thin films samples at 3.8 eV excitation energy.

The $Cs_2AgSb_xBi_{1-x}Br_6$ thin films were measured using TRMC at excitation energies of 3.8, 2.8, and 2.35 eV (325, 445, and 525 nm), with traces obtained at an excitation energy of 2.35 eV shown in Appendix Figure B.4. The traces obtained at excitation energies of 3.8 and 2.8 eV are shown in Figures 4.24 through 4.27. Like the $Cs_2AgBiBr_6$ thin films annealed at 90°C, the trap-filling behavior is absent

from the traces, indicating the same low crystallinity and high trap-assisted recombination.

An interesting result was that for all of the samples, the normalized maximum photoconductances at 2.8 eV excitation (within the excitonic peak) were nearly all of the same order of magnitude compared to at 3.8 eV excitation (well above the band gap). As discussed previously, this result could be explained by the amorphous nature of the films, with newly formed excitons contributing just as little to the conductance of the film as free charge carriers. However, the $Cs_2AgSb_{0.2}Bi_{0.8}Br_6$ sample experienced a significant decrease in maximum photoconductance (factor of 1/4) between excitation energies.

Comparing the maximal peak height position as a function of antimony substitution in Figure 4.21a), the excitation energy of 2.8 eV most closely aligns the absorbance peak of $Cs_2AgSb_{0.2}Bi_{0.8}Br_6$. This observation is consistent with a large fraction of excited electrons being in the form of excitons rather than free charge carriers, thus leading to a decrease in TRMC signal compared to excitation at 3.8 eV. While the excitation energies were set to 2.8 eV across all samples for consistency, it may be interesting to see the results of TRMC measurements with excitation energies set precisely to the maximal peak height energy of each sample as per the absorbance spectra. The contribution of the excitonic transition to the absorbance appears to be a relatively narrow peak, and exciting electrons at slightly different energies may produce dramatically different ratios of free charge carriers versus excitons in the thin film.

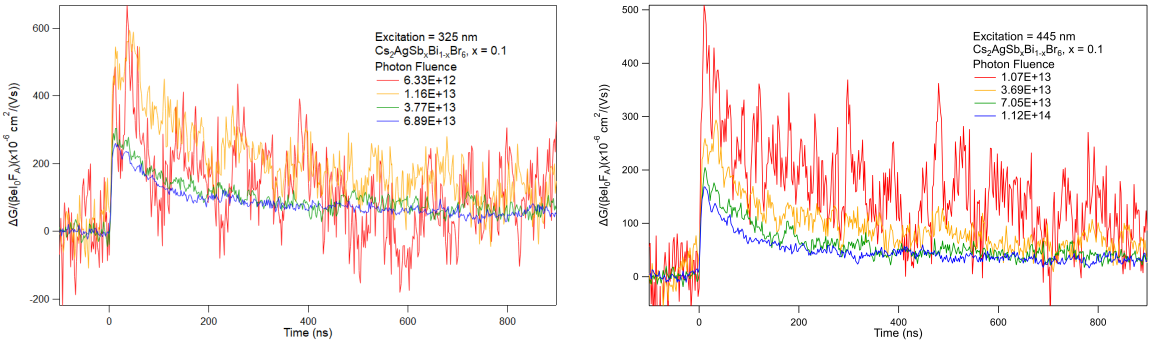

(a) Excitation = 325 nm (3.8 eV). **(b) Excitation = 445 nm (2.8 eV).**

Figure 4.24: TRMC traces of $Cs_2AgSb_{0.1}Bi_{0.9}Br_6$ annealed at 90°C.

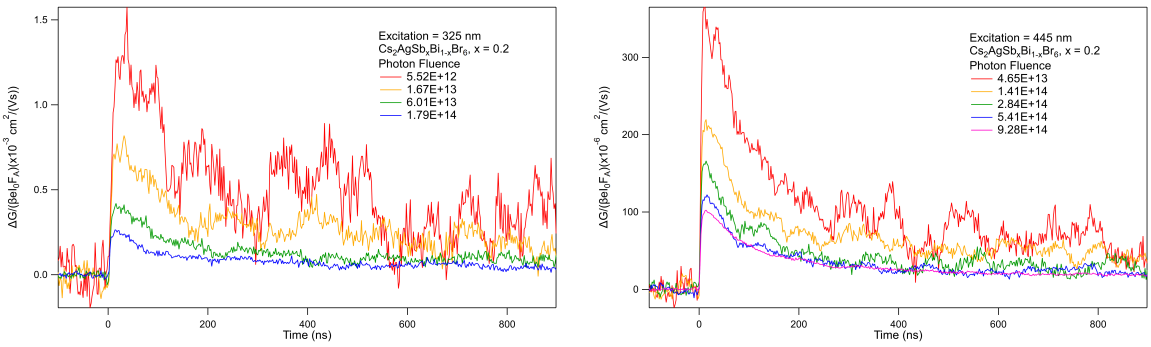

(a) Excitation = 325 nm (3.8 eV). **(b) Excitation = 445 nm (2.8 eV).**

Figure 4.25: TRMC traces of $Cs_2AgSb_{0.2}Bi_{0.8}Br_6$ annealed at 90°C.

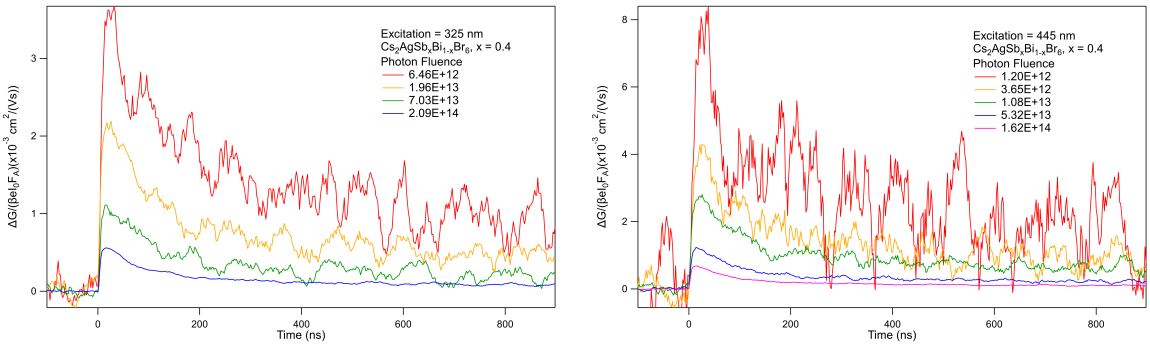

(a) Excitation = 325 nm (3.8 eV). **(b) Excitation = 445 nm (2.8 eV).**

Figure 4.26: TRMC traces of $Cs_2AgSb_{0.4}Bi_{0.6}Br_6$ annealed at 90°C.

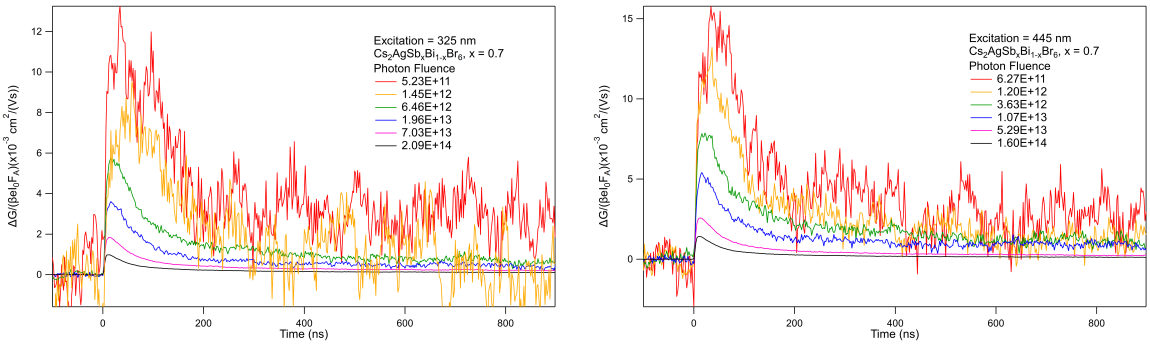

(a) Excitation = 325 nm (3.8 eV). **(b) Excitation = 445 nm (2.8 eV).**

Figure 4.27: TRMC traces of $Cs_2AgSb_{0.7}Bi_{0.3}Br_6$ annealed at 90°C.

5

Conclusions and Recommendations

5.1. Conclusions

The solution chemistry of $BiBr_3$ in DMSO was explored via Density Functional Theory combined with experimental solution spectroscopy. The main transition found in Bi-Br-DMSO system was a metal-to-ligand charge transfer process involving the $6s$ orbital of bismuth and the $3p$ orbital of bromine, and was confirmed by molecular orbital diagram, the shape of the HOMO and LUMO surfaces, and the relatively large change in simulated absorbance peak energy upon use of longer-ranged functionals. The corner-sharing $[Bi_4Br_{20}]^{8-}$ complex was found to match the experimental absorbance peak at ~3.9 eV, but no complex was found to match the transition at 3.5 eV. The inclusion of Cs^{1+} ions had very little effect on the simulated absorbance spectra of the Bi-Br-DMSO complexes, which was consistent with experimental results. However, geometry calculations showed optimized structures with Cs^{1+} ions sitting in the cavity of three bromine ions in a geometry echoing that of the double perovskite crystal structure, indicating the liklihood of the double perovskite crystallite formation in the sequential precursor dissolution pathway.

Experimentally, the facile synthesis method of dissolving all precursors together in DMSO and spin coating to create a $Cs_2AgSb_xBi_{1-x}Br_6$ double perovskite was accomplished, with variables such as the amount of antimony substitution and annealing temperature tested to determine a preferred synthesis route. Higher annealing temperatures, though more crystalline when observed under SEM, tended to introduce degradation products (visible as extra reflections of BiOBr in the diffractogram) and did not incorporate antimony into the lattice at any concentration. A low annealing temperature of 90°C was found to incorporate an antimony substitution of up to 70% without degradation upon exposure to air, at the cost of crystallinity and optoelectronic performance. The substitution of Bi^{3+} for Sb^{3+} led to a change in the band gap from 2.27 eV to 2.07 eV (based on the onset of absorption) and a decrease in the lattice parameter of ~0.05 Å (via XRD measurements). These results were consistent with the smaller Sb^{3+} ion replacing the larger Bi^{3+} ion in the crystal structure. TRMC measurements confirmed that the more crystalline thin films annealed at higher temperatures had longer charger carrier lifetimes and higher normalized maximum photoconductance than the less crystalline thin films annealed at lower temperatures. The reason for this discrepancy was hypothesized to be a result of excessive trap-assisted recombination, which was also the reason for trap-filling behavior not being observed in thin films annealed at lower temperatures. Low-temperature absorbance measurements showed a trend of increasing absorbance peak height with decreasing temperature, contrary to what would be expected from scattering via electron-phonon coupling. Further TRMC measurements on the thin films annealed at high temperatures using an excitation energy of 2.8 eV (445 nm) resulted in a decrease in photoconductance signal, and indicated that the transition was most likely the result of an excitonic transition, as a result of a larger proportion of electrons being excited to excitons rather than free charge carriers.

5.2. Recommendations for Future Work

5.2.1. Computational

A portion of the computational work which could be redone would be obtaining the solution spectra with the right equipment. The solutions absorbed both much more strongly and at much higher energies than the thin films, requiring a different set of equipment to properly obtain solution spectra. An ultra-low path length (10 µm) cuvette should be used so that the solutions do not require serial dilution to provide a usable signal to the detector. A different spectrophotometer and detector with a better measurement range in the UV regime should be used as well. This could reveal the precise location of the peak located between ~4.5-5.5 eV and, when combined with DFT calculations of simulated spectra, could help identify the complexes in solution.

Extension of the computational work offers multiple possibilities. As mentioned, Bi-Br-Cs-DMSO complexes were already studied, leaving only the addition of the AgBr precursor to create the double perovskite. Understanding the conditions required to properly form the double perovksite phase with precisely alternating Ag^{1+} and Bi^{3+} ions is a possible avenue for study. Additionally, the Bi-Br-Cs-Ag-DMSO complexes found to be most stable could be analyzed using TD-DFT to match their simulated absorbance peaks to the experimentally obtained spectra of double perovskite spin coating solution used for synthesis, leading to an enhanced understanding of the double perovskite synthesis.

Another route for further study would be to continue the work presented in this report on $SbBr_3$ in solution, which showed the same dissolution patterns as $BiBr_3$ (dissolving individually and with CsBr, but not with AgBr). Merging these results with the topic above would lead to a complete computational understanding of the solution phase synthesis of $Cs_2AgSb_xBi_{1-x}Br_6$.

5.2.2. Experimental

Additional experimental measurements which could support the hypotheses put forth in this report include absorbance measurements at low temperatures for the antimony substituted thin films. Figure 4.21a shows that not only does the peak position change with antimony substitution, but that the peak strength changes as well. This may indicate a lower exciton binding energy as antimony content increases, and examining the behavior of the thin films at low temperatures could help understand how the contribution of the excitonic transition to the absorbance spectra changes with antimony substitution. On the same line of reasoning, TRMC measurements with excitations at the precise absorbance peak energy could also help to quantify the contribution of the excitonic transition to the absorbance spectra. Comparing charge carrier dynamics and free charge carrier generation over a range of excitation energies from the excitonic peak energy to an energy well above the band gap should allow for comparison of the proportion of free charges versus excitons upon photoexcitation.

On a more device-focused track, the synthesis of $Cs_2AgSb_xBi_{1-x}Br_6$ could be fine tuned by varying the annealing conditions to try and see if a balance can be found between having a highly crystalline sample with good optoelectronic properties and incorporating antimony into the crystal structure. Full double perovskite PV cells could also be synthesized to examine how well charge carriers transport at the interface of the various layers required to form a PV cell.

Bibliography

[1] John Perlin, National Renewable Energy Laboratory. The Silicon Solar Cell Turns 50. https://www.nrel.gov/docs/fy04osti/33947.pdf, 2004.

[2] Gavin Conibeer. Third-generation photovoltaics. *Materials Today*, 10(11):42–50, 2007. doi: 10.1016/S1369-7021(07)70278-X.

[3] Po-Kai Kung, Ming-Hsien Li, Pei-Ying Lin, Jia-Yun Jhang, Martina Pantaler, Doru C. Lupascu, Giulia Grancini, and Peter Chen. Lead-Free Double Perovskites for Perovskite Solar Cells. *Solar RRL*, 4(2):1900306, 2019. doi: 10.1002/solr.201900306.

[4] Michael M. Lee, Joël Teuscher, Tsutomu Miyasaka, Takurou N. Murakami, and Henry J. Snaith. Efficient Hybrid Solar Cells Based on Meso-Superstructured Organometal Halide Perovskites. *Science*, 338(6107):643–647, 2012. doi: 10.1126/science.1228604.

[5] Julian Burschka, Norman Pellet, Soo-Jin Moon, Robin Humphry-Baker, Peng Gao, Mohammad K. Nazeeruddin, and Michael Grätzel. Sequential deposition as a route to high-performance perovskite-sensitized solar cells. *Nature*, 499:316–319, 2013. doi: 10.1038/nature12340.

[6] National Renewable Energy Laboratory. Best Research-Cell Efficiencies. https://www.nrel.gov/pv/assets/pdfs/best-research-cell-efficiencies.20200708.pdf, 2020.

[7] Samuel D. Stranks, Giles E. Eperon, Giulia Grancini, Christopher Menelaou, Marcelo J. P. Alcocer, Tomas Leijtens, Laura M. Herz, Annamaria Petrozza, and Henry J. Snaith. Electron-Hole Diffusion Lengths Exceeding 1 Micrometer in an Organometal Trihalide Perovskite Absorber. *Science*, 342 (6156):341–344, 2013. doi: 10.1126/science.1243982.

[8] Andy Extance. Perovskites on Trial. *Nature*, 570:429–432, 2019. doi: 10.1038/d41586-019-01985-y.

[9] Guangda Niu, Xudong Guo and Liduo Wang. Review of recent progress in chemical stability of perovskite solar cells. *Journal of Materials Chemistry A*, 3:8970–8980, 2015. doi: 10.1039/c4ta04994b.

[10] Agency for Toxic Substances and Disease Registry, Centers for Disease Control and Prevention. Lead Toxicity. https://www.atsdr.cdc.gov/csem/lead/docs/CSEM-Lead_toxicity_508.pdf, 2017.

[11] Office of the Law Revision Counsel of the United States House of Representatives. 42 U.S.C. 4852d - Disclosure of information concerning lead upon transfer of residential property. https://www.govinfo.gov/content/pkg/USCODE-2009-title42/pdf/USCODE-2009-title42-chap63A-subchapI-sec4852d.pdf, 2009.

[12] European Union. Directive 98/70/EC of the European Parliament and of the Council of 13 October 1998 relating to the quality of petrol and diesel fuels and amending Council Directive 93/12/EE. https://eur-lex.europa.eu/legal-content/EN/TXT/PDF/?uri=CELEX:01998L0070-20181224&from=EN, 1998.

[13] Tomas Leijtens, Rohit Prasanna, Aryeh Gold-Parker, Michael F. Toney, and Michael D. McGehee. Mechanism of Tin Oxidation and Stabilization by Lead Substitution in Tin Halide Perovskites. *ACS Energy Letters*, 2(9):2159–2165, 2017. doi: 10.1021/acsenergylett.7b00636.

[14] Nakita K. Noel, Samuel D. Stranks, Antonio Abate, Christian Wehrenfennig, Simone Guarnera, Amir-Abbas Haghighirad, Aditya Sadhanala, Giles E. Eperon, Sandeep Pathak, Michael B. Johnston, Annamaria Petrozza, Laura M. Herza, and Henry J. Snaith. Lead-free organic–inorganic tin halide perovskites for photovoltaic applications. *Energy & Environmental Science*, 7:3061–3068, 2014. doi: 10.1039/C4EE01076K.

[15] Adam H. Slavney, Te Hu, Aaron M. Lindenberg, and Hemamala I. Karunadasa. A Bismuth-Halide Double Perovskite with Long Carrier Recombination Lifetime for Photovoltaic Applications. *Journal of the American Chemical Society*, 138:2138–2141, 2016. doi: 10.1021/jacs.5b1329.

[16] William Shockley, and Hans J. Queisser. Detailed Balance Limit of Efficiency of p-n Junction Solar Cells. *Journal of Applied Physics*, 32(3):510–519, 1960. doi: 10.1063/1.1736034.

[17] Fuxiang Ji, Johan Klarbring, Feng Wang, Weihua Ning, Linqin Wang, Chunyang Yin, José Silvestre Mendoza Figueroa, Christian Kolle Christensen, Martin Etter, Thomas Ederth, Licheng Sun, Sergei I. Simak, Igor A. Abrikosov, and Feng Gao. Lead□Free Halide Double Perovskite $Cs_2AgBiBr_6$ with Decreased Band Gap. *Angewandte Chemie*, 59(35):15191–15194, 2020. doi: 10.1002/anie.202005568.

[18] Eline M. Hutter, María C. Gélvez-Rueda, Davide Bartesaghi, Ferdinand C. Grozema, and Tom J. Savenije. Band-Like Charge Transport in $Cs_2AgBiBr_6$ and Mixed Antimony–Bismuth $Cs_2AgBi_{1-x}Sb_xBr_6$ Halide Double Perovskites. *ACS Omega*, 3(9):11655–11662, 2018. doi: 10.1021/acsomega.8b01705.

[19] Ke-zhao Du, Weiwei Men, Xiaoming Wang, Yanfa Yan, and David B. Mitzi. Bandgap Engineering of Lead-Free Double Perovskite $Cs_2AgBiBr_6$ through Trivalent Metal Alloying. *Angewandte Chemie*, 56(28):8158–8162, 2017. doi: 10.1002/anie.201703970.

[20] Gonzalo García-Espejo, Daily Rodríguez-Padrón, Rafael Luque, Luis Camacho, and Gustavo de Miguel. Mechanochemical synthesis of three double perovskites: $Cs_2AgBiBr_6$, $(CH_3NH_3)_2TlBiBr_6$ and $Cs_2AgSbBr_6$. *Nanoscale*, 11:16650–16657, 2019. doi: 10.1039/c9nr06092h.

[21] Femi Igbari, Rui Wang, Zhao-Kui Wang, Xing-Juan Ma, Qiang Wang, Kai-Li Wang, Yue Zhang, Liang-Sheng Liao, and Yang Yang. Composition Stoichiometry of $Cs_2AgBiBr_6$ Films for Highly Efficient Lead-Free Perovskite Solar Cells. *Nano Letters*, 19:2066–2073, 2019. doi: 10.1021/acs.nanolett.9b00238.

[22] Enrico Greul, Michiel L. Petrus, Andreas Binek, Pablo Docampo, and Thomas Bein. Highly stable, phase pure $Cs_2AgBiBr_6$ double perovskite thin films for optoelectronic applications. *Journal of Materials Chemistry A*, 5:19972—19981, 2017. doi: 10.1039/c7ta06816f.

[23] Ping Fan, Huan-Xin Peng, Zhuang-Hao Zheng, Zi-Hang Chen, Shi-Jie Tan, Xing-Ye Chen,Yan-Di Luo, Zheng-Hua Su, Jing-Ting Luo, and Guang-Xing Liang. Single-Source Vapor-Deposited $Cs_2AgBiBr_6$ Thin Films for Lead-Free Perovskite Solar Cells. *Nanomaterials*, 9(1760), 2019. doi: 10.3390/nano9121760.

[24] Ming Wang, Peng Zeng, Sai Bai, Jinwen Gu, Faming Li, Zhou Yang, and Mingzhen Liu. High-Quality Sequential-Vapor-Deposited $Cs_2AgBiBr_6$ Thin Films for Lead-Free Perovskite Solar Cells. *Solar RRL*, 2(12):1800217, 2018. doi: 10.1002/solr.201800217.

[25] Zewei Li, Sean Kavanagh, Mari Napari, Robert G. Palgrave, Mojtaba Abdi-Jalebi, Zahra Andaji-Garmaroudi, Daniel W. Davies, Mikko Laitinen, Jaakko Julin, Richard H. Friend, David O. Scanlon, Aron Walsh, and Robert L. Z. Hoye. Bandgap Lowering in Mixed Alloys of $Cs_2Ag(SbCs_xBiCs_{1-x})BrCs_6$ Double Perovskite Thin Films, 2020.

[26] Yuan Liu, Li Zhang, Min Wang, Yujia Zhong, Meirong Huang, Yu Long, Hongwei Zhu. Bandgap-tunable double-perovskite thin films by solution processing. *Materials Today*, 28:25–30, 2019. doi: 10.1016/j.mattod.2019.04.023.

[27] Donald A. Neaman. *Semiconductor Physics and Devices: Basic Principles*. McGraw-Hill, New York, New York, 4th edition, 2012.

[28] Arjan Jeroen Houtepen. *Charge injection and transport in quantum confined and disordered systems*. PhD thesis, Utrecht University, 2007.

[29] Manijeh Razeghi. *Electron Phonon Interactions*, pages 1–10. Springer US, Boston, Massachusetts, 2009. ISBN 978-0-387-92168-6. doi: 10.1007/978-0-387-92168-6_14.

[30] Mildred Dresselhaus, Gene Dresselhaus, Stephen B. Cronin, and Antonio Gomes Souza Filho. *Electron and Phonon Scattering*, pages 185–209. Springer Berlin Heidelberg, Berlin, Heidelberg, 2018. ISBN 978-3-662-55922-2. doi: 10.1007/978-3-662-55922-2_9.

[31] Yu-Che Hsiao, Ting Wu, Mingxing Li, Qing Liu, Wei Qin, and Bin Hu. Fundamental physics behind high-efficiency organo-metal halide perovskite solar cells . *Journal of Materials Chemistry A*, 3 (30):15372–15385, 2015. doi: 10.1039/C5TA01376C.

[32] Robin Kentsch, Mirko Scholz, Jonas Horn, Derck Schlettwein, Kawon Oum, and Thomas Lenzer. Exciton Dynamics and Electron-Phonon Coupling Affect the Photovoltaic Performance of the $Cs_2AgBiBr_6$ Double Perovskite. *Journal of Physical Chemistry C*, 122(45):25940—25947, 2018. doi: 10.1021/acs.jpcc.8b09911.

[33] S. J. Zelewski, J. M. Urban, A. Surrente, D. K. Maude, A. Kuc, L. Schade, R. D. Johnson, M. Dollmann, P. K. Nayak, H. J. Snaith, P. Radaelli, R. Kudrawiec, R. J. Nicholas, P. Plochocka, and M. Baranowski. Revealing the nature of photoluminescence emission in the metal-halide double perovskite $Cs_2AgBiBr_6$. *Journal of Materials Chemistry C*, 7(27):8350–8356, 2019. doi: 10.1039/c9tc02402f.

[34] R.D. Shannon. Revised Effective Ionic Radii and Systematic Studies of Interatomic Distances in Halides and Chalcogenides. *Acta Crystallographica Section A*, 32:751–767, 1976. doi: 10.1107/S0567739476001551.

[35] Isabella de Arandas Silva, Willian X. C. Oliveira, Ana Flávia Nogueira. Lead-free Perovskite Cs_2AgBiI_6 thin film prepared by Ion Exchange of $Cs_2AgBiBr_6$ thin films. In *Proceedings of 42a Reunião Anualda Sociedade Brasileira de Química*, 2019.

[36] Zewen Xiao, Weiwei Meng, Jianbo Wang, and Yanfa Yan. Thermodynamic Stability and Defect Chemistry of Bismuth-Based Lead-Free Double Perovskites. *ChemSusChem*, 9(18):2628–2633, 2016. doi: 10.1002/cssc.201600771.

[37] Xin-Gang Zhao, Ji-Hui Yang, Yuhao Fu, Dongwen Yang, Qiaoling Xu, Liping Yu, Su-Huai Wei, and Lijun Zhang. Design of Lead-Free Inorganic Halide Perovskites for Solar Cells via Cation-Transmutation. *Journal of the American Chemical Society*, 139(7):2630–2638, 2017. doi: 10.1021/jacs.6b09645.

[38] Pierre Hohenberg and Walter Kohn. Inhomogeneous Electron Gas. *Physical Review*, 136(3B): 864–871, 1964. doi: 10.1103/PhysRev.136.B864.

[39] Software for Chemistry & Materials B.V. ADF Manual. `https://www.scm.com/doc/ADF/index.html`, 2019.

[40] Zimu Wei, Dengyang Guo, Jos Thieme, Claudine Katan, Valentina M. Caselli, Jacky Even, and Tom J. Savenije. The importance of relativistic effects on two-photon absorption spectra in metal halide perovskites. *Nature Communications*, 10(5342), 2019. doi: 10.1038/s41467-019-13136-y.

[41] Dariusz Kedziera, Monika Stanke, Sergiy Bubin, Maria Barysz, and Ludwik Adamowicz. Darwin and mass-velocity relativistic corrections in non-Born-Oppenheimer variational calculations. *The Journal of Chemical Physics*, 125(084303), 2006. doi: 10.1063/1.2236113.

[42] Takeshi Yanai, David P. Tew, Nicholas C. Handy. A new hybrid exchange–correlation functional using the Coulomb-attenuating method (CAM-B3LYP). *Chemical Physics Letters*, 393(1–3):51–57, 2004. doi: 10.1016/j.cplett.2004.06.011.

[43] Fengxia Wei, Zeyu Deng, Shijing Sun, Noor Titan Putri Hartono, Hwee Leng Seng, Tonio Buonassisi, Paul D. Bristowe, and Anthony K. Cheetham. Enhanced visible light absorption for lead-free double perovskite $Cs_2AgSbBr_6$. *Chemical Communications*, 55:3721–3724, 2019. doi: 10.1039/c9cc01134j.

[44] Robert L. Z. Hoye, Lissa Eyre, Fengxia Wei, Federico Brivio, Aditya Sadhanala, Shijing Sun, Weiwei Li, Kelvin H. L. Zhang, Judith L. MacManus-Driscoll, Paul D. Bristowe, Richard H. Friend, Anthony K. Cheetham, and Felix Deschler. Fundamental Carrier Lifetime Exceeding 1 µs in $Cs_2AgBiBr_6$ Double Perovskite. *Advanced Materials Interfaces*, 5(1800464), 2018. doi: 10.1002/admi.201800464.

[45] Peter Atkins and Julio de Paula. *Physical Chemistry*. Oxford University Press, New York, New York, Ninth edition, 1993.

[46] Perkin Elmer, Inc. LAMBDA 1050+ Interactive Brochure. https://www.perkinelmer.com/lab-solutions/resources/docs/bro_013833_01_lambda_1050-plus_uv-vis-nir.pdf, 2018–2019.

[47] Jan Tauc. Optical Properties and Electronic Structure of Amorphous Ge and Si. *Materials Research Bulletin*, 3(1):37–46, 1968. doi: 10.1016/0025-5408(68)90023-8.

[48] Tom J. Savenije, Andrew J. Ferguson, Nikos Kopidakis, and Garry Rumbles. Revealing the Dynamics of Charge Carriers in Polymer:Fullerene Blends Using Photoinduced Time-Resolved Microwave Conductivity. *Journal of Physical Chemistry C*, 117(46):24085—24103, 2013. doi: 10.1021/jp406706u.

[49] Jessica E.Kroeze, Tom J.Savenije, and John M.Warman. Exciton diffusion and interfacial charge separation in photovoltaic materials studied by microwave conductivity. *Comptes Rendus Chimie*, 9(5–6):667–675, 2006. doi: 10.1016/j.crci.2005.03.022.

[50] Laura Schade, Adam D. Wright, Roger D. Johnson, Markus Dollmann, Bernard Wenger, Pabitra K. Nayak, Dharmalingam Prabhakaran, Laura M. Herz, Robin Nicholas, Henry J. Snaith, and Paolo G. Radaelli. Structural and Optical Properties of $Cs_2AgBiBr_6$ Double Perovskite. *ACS Energy Letters*, 4(1):299–305, 2018. doi: 10.1021/acsenergylett.8b02090.

[51] Krzysztof Iniewski, editor. *Semiconductor Radiation Detection Systems*. CRC Press, Boca Raton, Florida, 1st edition, 2010.

A

Appendix – Computational

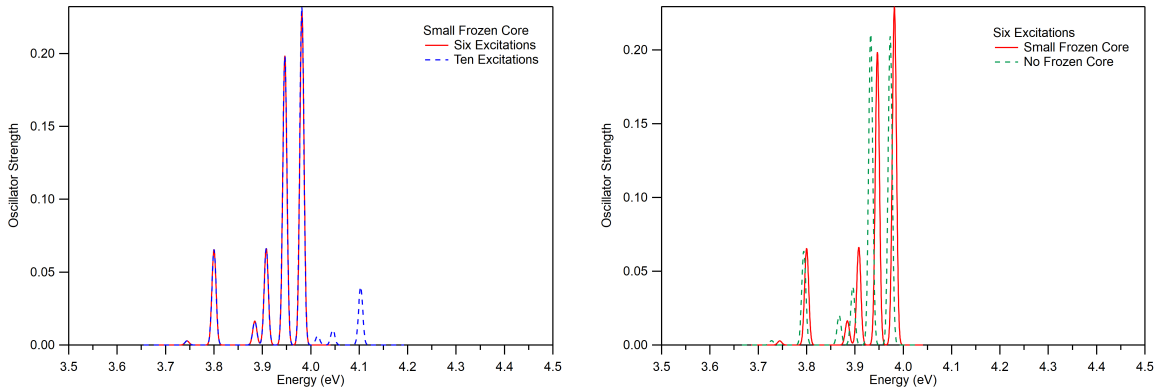

(a) Effect of number of excitations. **(b) Effect of frozen core.**

Figure A.1: The effects of changing a) The number of excitations resulting in the addition of higher energy, lower probability peaks, and b) the effect of removing the frozen core option resulting in a small energy shift.

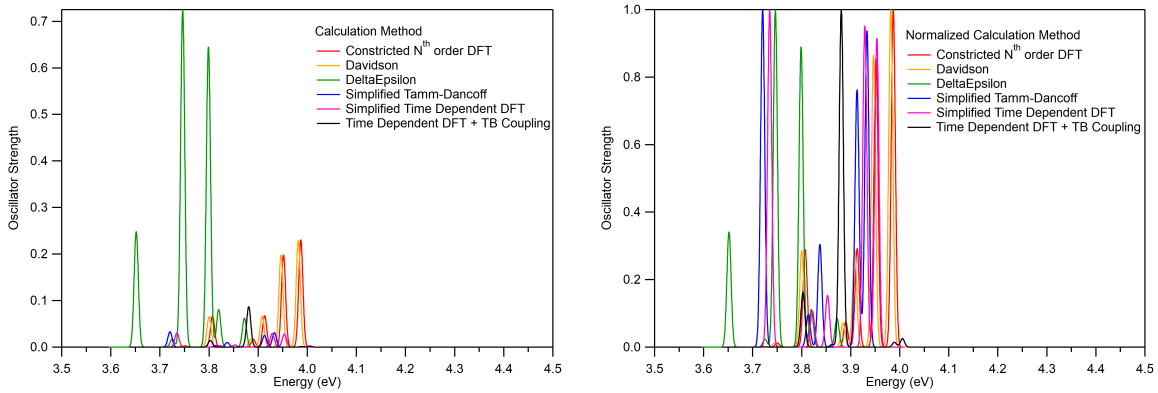

(a) Different methods, unnormalized. **(b) Different methods, maximum value normalized to 1.**

Figure A.2: The effect of changing the calculation method used for the simulated absorbance spectra, both normalized and unnormalized.

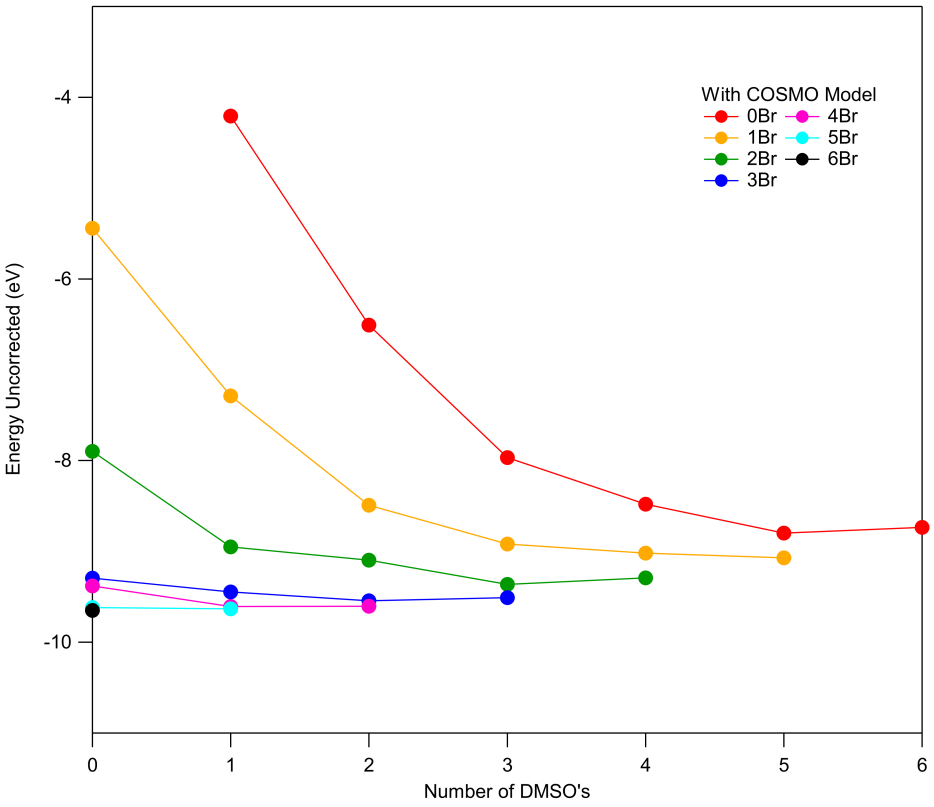

Figure A.3: Plot of the uncorrected interaction energy for Sb-Br-DMSO complexes. Calculated using the same settings as for the Bi-Br-DMSO complex geometry optimizations (BLYP functional, TZP basis set, COSMO model, small frozen core, scalar relativity).

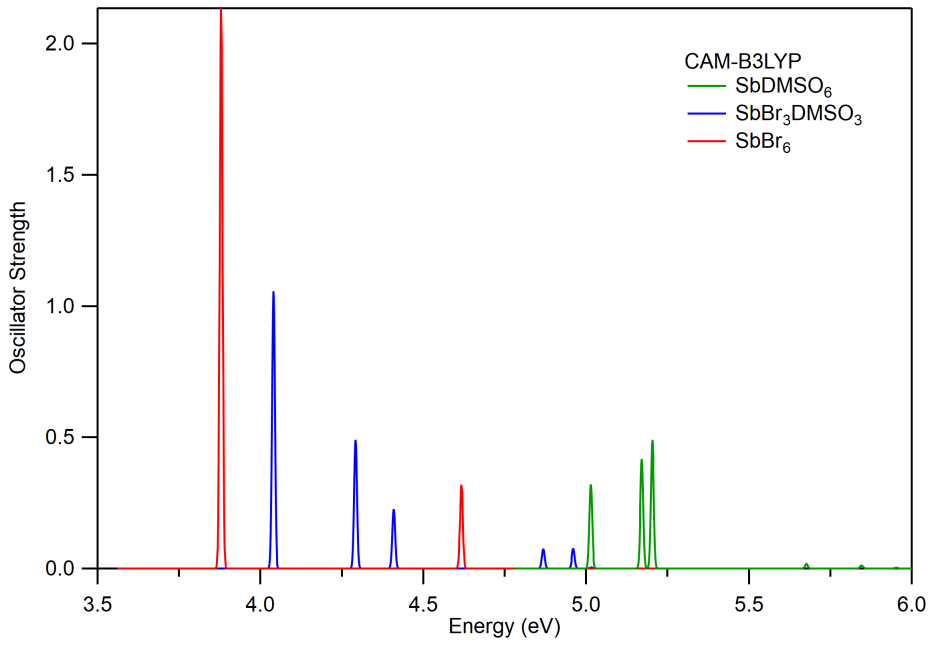

Figure A.4: Plot of the simulated absorbance spectra for six-coordinated Sb-Br-DMSO complexes (CAM-B3LYP functional, TZP basis set, COSMO model, small frozen core, scalar relativity). The trend was the same as for the Bi-Br-DMSO complexes, which was a decrease in simulated transition energies as Br^{1-} replaced DMSO ligands.

Table A.1: Table of individual fragment energy values for calculation of interaction energy with COSMO. Note that the fragment energies of DMSO and Br^{1-} remained more or less constant throughout, but the fragment energy of Bi^{3+} increased by ~2 eV per ligand added to the complex. Without COSMO, all fragment energies remained more or less constant, regardless of the number of ligands.

		Energy of complex with all other ions ghosted (eV)													Interaction Energy (eV)		
Molecule or Fragment	Total Bonding Energy (eV)	Bi	DMSO #1	DMSO #2	DMSO #3	DMSO #4	DMSO #5	DMSO #6	Br #1	Br #2	Br #3	Br #4	Br #5	Br #6	Corrected	Uncorrected	BSSE (eV)
Bi^{3+}	17.71																
Br^{1-}	-6.38																
DMSO	-47.75																
$BiDMSO_1$	-33.71	18.74	-47.17												-5.28	-3.67	-1.61
$BiDMSO_2$	-83.61	20.25	-47.25	-47.11											-9.49	-5.81	-3.68
$BiDMSO_3$	-132.76	22.51	-47.28	-47.20	-47.23										-13.56	-7.21	-6.34
$BiDMSO_4$	-181.12	24.27	-47.25	-47.35	-47.33	-47.22									-16.22	-7.81	-8.41
$BiDMSO_5$	-229.34	27.11	-47.19	-47.37	-47.32	-47.28	-47.27								-20.03	-8.28	-11.75
$BiDMSO_6$	-277.35	31.77	-47.26	-47.28	-47.25	-47.32	-47.27	-47.30							-25.43	-8.53	-16.90
$BiBr_1$	6.34	18.56							-6.34						-5.87	-4.99	-0.88
$BiBr_1DMSO_1$	-43.10	19.88	-47.35						-6.28						-9.36	-6.69	-2.68
$BiBr_1DMSO_2$	-92.04	21.75	-47.38	-47.37					-6.20						-12.84	-7.87	-4.97
$BiBr_1DMSO_3$	-140.27	23.85	-47.39	-47.31	-47.36				-6.19						-15.86	-8.34	-7.53
$BiBr_1DMSO_4$	-188.42	26.05	-47.21	-47.37	-47.45	-47.32			-6.10						-19.03	-8.74	-10.29
$BiBr_1DMSO_5$	-236.30	30.71	-47.34	-47.28	-47.37	-47.38	-47.31		-6.03						-24.30	-8.86	-15.44
$BiBr_2$	-2.40	19.63							-6.32	-6.32					-9.40	-7.36	-2.04
$BiBr_2DMSO_1$	-51.17	21.42	-47.41						-6.25	-6.28					-12.65	-8.37	-4.28
$BiBr_2DMSO_2$	-99.11	23.48	-47.32	-47.31					-6.21	-6.21					-15.54	-8.56	-6.98
$BiBr_2DMSO_3$	-147.27	25.48	-47.38	-47.46	-47.46				-6.23	-6.10					-18.12	-8.97	-9.16
$BiBr_2DMSO_4$	-195.21	29.72	-47.36	-47.41	-47.41	-47.33			-6.06	-6.06					-23.29	-9.15	-14.14
$BiBr_3$	-10.19	21.03							-6.30	-6.29	-6.29				-12.33	-8.77	-3.56
$BiBr_3DMSO_1$	-58.20	22.62	-47.56						-6.23	-6.23	-6.28				-14.52	-9.02	-5.50
$BiBr_3DMSO_2$	-106.17	24.92	-47.47	-47.47					-6.24	-6.16	-6.17				-17.58	-9.24	-8.34
$BiBr_3DMSO_3$	-154.04	28.93	-47.38	-47.42	-47.38				-6.14	-6.18	-6.07				-22.40	-9.35	-13.05
$BiBr_4$	-16.96	22.70							-6.30	-6.30	-6.30	-6.30			-14.46	-9.16	-5.30
$BiBr_4DMSO_1$	-64.90	24.60	-47.50						-6.26	-6.22	-6.25	-6.22			-17.05	-9.34	-7.71
$BiBr_4DMSO_2$	-112.76	28.28	-47.44	-47.44					-6.16	-6.20	-6.16	-6.09			-21.54	-9.44	-12.09
$BiBr_5$	-23.57	24.37							-6.25	-6.27	-6.26	-6.27	-6.26		-16.62	-9.39	-7.24
$BiBr_5DMSO_1$	-71.42	27.68	-47.46						-6.22	-6.18	-6.21	-6.21	-6.17		-20.64	-9.49	-11.15
$BiBr_6$	-30.10	26.99							-6.24	-6.24	-6.24	-6.24	-6.24	-6.24	-19.66	-9.54	-10.12

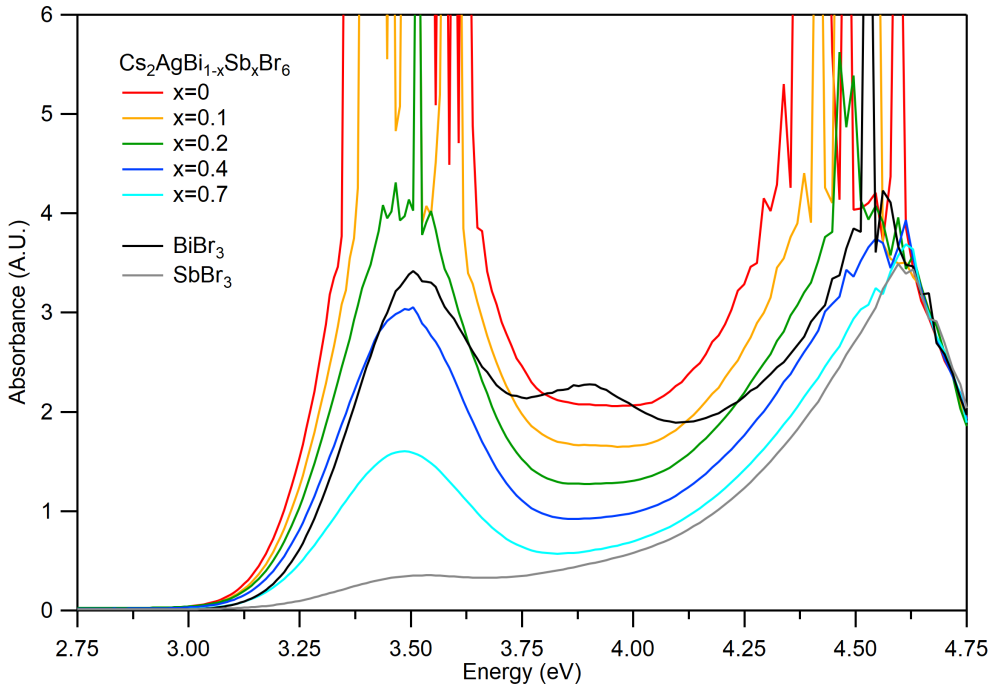

Figure A.5: Experimental absorbance spectra of solutions of all precursors together, overlaid with the absorbance spectra of individual $BiBr_3$ and $SbBr_3$. While the peak at 3.5 eV persists in the double perovskite solution, the peak at 3.9 eV was absent, suggesting that whatever Bi-Br-DMSO complex was present and absorbing at that energy was somehow removed from solution by the addition of the other precursors. As $SbBr_3$ content increased, the spectrum of the double perovskite solution resembled that of $BiBr_3$ less, and that of $SbBr_3$ more.

B

Appendix – Experimental

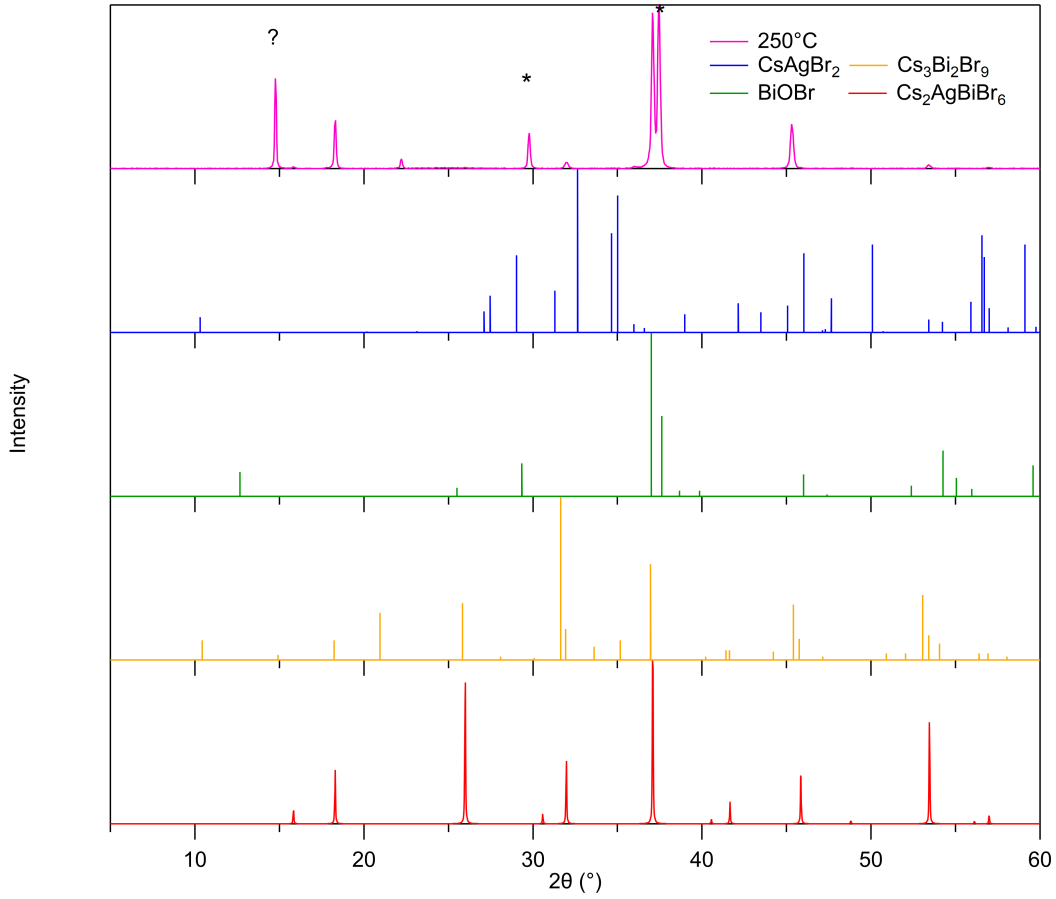

Figure B.1: $Cs_2AgBiBr_6$ annealed at 250°C compared to common side product reference diffractograms.

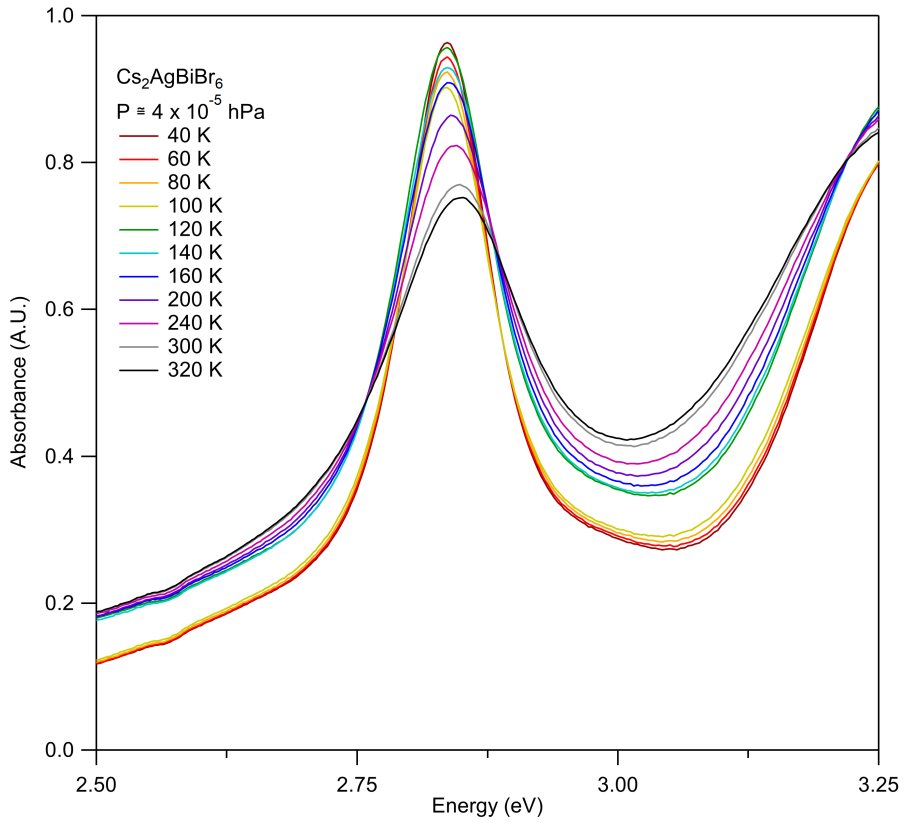

Figure B.2: Unshifted absorbance spectra of $Cs_2AgBiBr_6$ at low temperatures. There was a noticeable difference in the curves above and below the tetragonal phase shift temperature of ~120°C, likely due to the structural changes in the material. The absorbance peak narrows and becomes taller as the temperature decreases, but does not disappear, supporting the hypothesis that the transition was excitonic in nature and not a result of scattering via electron-phonon coupling.

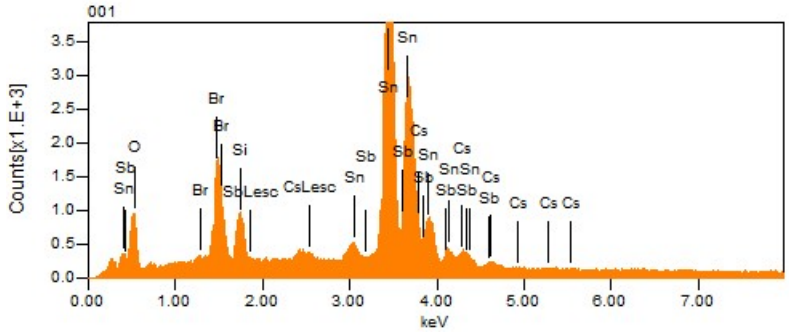

Figure B.3: EDXS output of $Cs_2AgSb_{0.4}Bi_{0.6}Br_6$ with the characteristic peaks labelled. The peaks ascribed to antimony were overlapped by the large signal from tin in the same energy range.

Table B.1: Thicknesses of thin films annealed at 90°C measured using the Dektak profilometer.

Sb^{3+} Content (x value)	Average Sample Height (nm)	Average Roughness (nm)
0	195.36 ± 25.36	38.98 ± 14.81
0.1	236.62 ± 16.87	36.83 ± 9.78
0.2	299.62 ± 100.51	58.55 ± 18.49
0.4	255.16 ± 32.32	70.24 ± 29.26
0.7	212.76 ± 38.82	51.50 ± 25.87

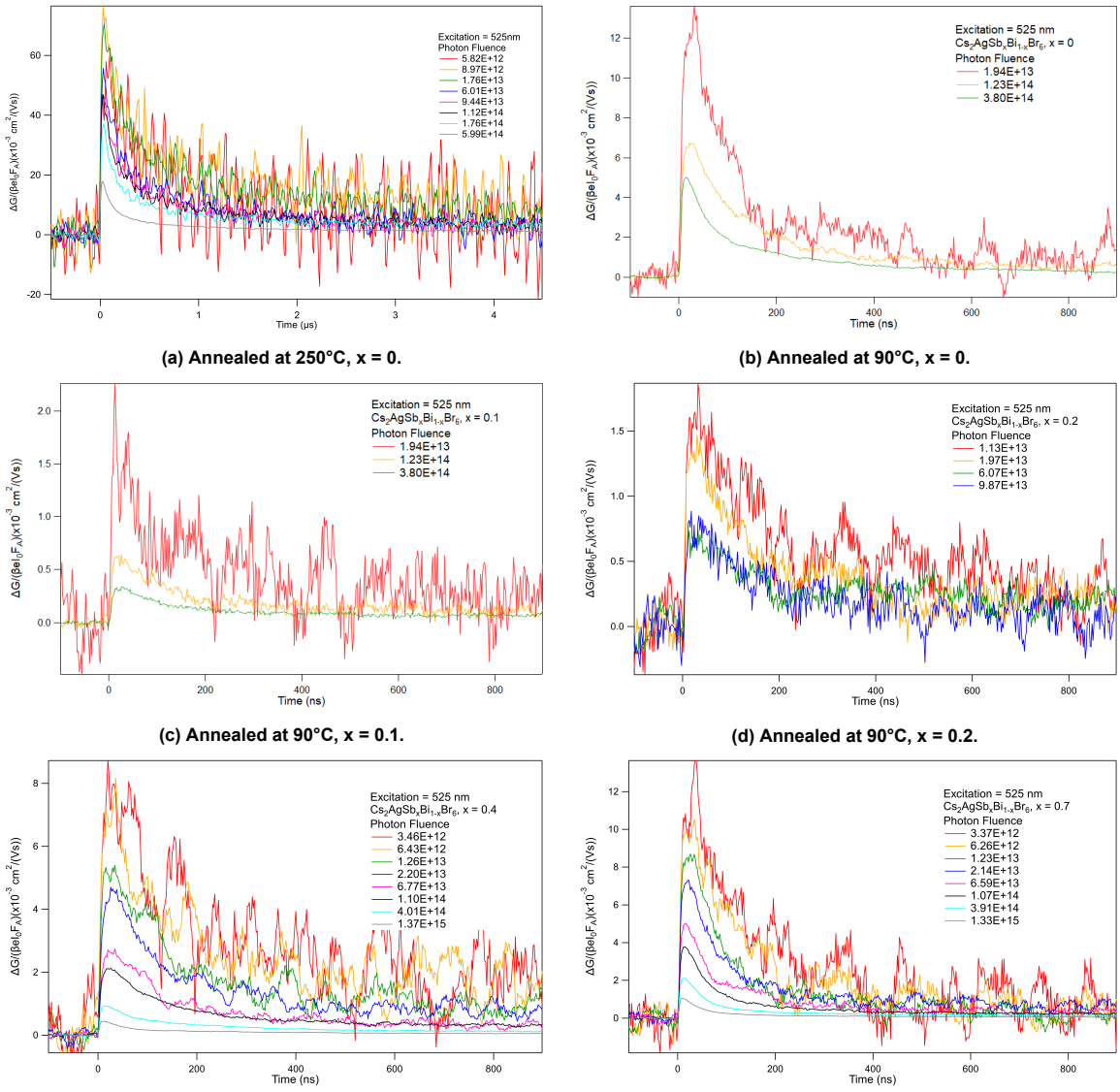

(a) Annealed at 250°C, x = 0.

(b) Annealed at 90°C, x = 0.

(c) Annealed at 90°C, x = 0.1.

(d) Annealed at 90°C, x = 0.2.

(e) Annealed at 90°C, x = 0.4.

(f) Annealed at 90°C, x = 0.7.

Figure B.4: TRMC plots of $Cs_2AgSb_xBi_{1-x}Br_6$ using an excitation energy of 3.8 eV (525 nm). Because the absorbance of the double perovskite thin films is low at this wavelength (<0.15 A.U.), the plots have significant error (the result of the signals being normalized by a small number), and as such have been relegated to the Appendix. Like the plots in the main text, the sample annealed at 250°C has a longer charge carrier lifetime and thus was measured on a longer time scale.